nature communications

Article

https://doi.org/10.1038/s41467-024-54628-w

Multi-protomics analysis identified host cellular pathways perturbed by tick-borne encephalitis virus infection

Received: 9 March 2024

Accepted: 15 November 2024

Published online: 30 November 2024

Check for updates

Liyan Sui[1,8], Wenfang Wang[1,2,8], Xuerui Guo[3], Yinghua Zhao[1], Tian Tian[2], Jinlong Zhang[3], Heming Wang[4], Yueshan Xu[5], Hongmiao Chi[1], Hanxi Xie[2], Wenbo Xu[1], Nan Liu[1], Li Zhao[1], Guangqi Song[4], Zedong Wang[1], Kaiyu Zhang[1], Lihe Che[1], Yicheng Zhao[1,5,6] ✉, Guoqing Wang[2] ✉ & Quan Liu[1,7] ✉

Tick-borne encephalitis virus (TBEV) represents a pivotal tick-transmitted flavivirus responsible for severe neurological consequences in Europe and Asia. The emergence of TBEV genetic mutations and vaccine-breakthrough infections, along with the absence of effective vaccines and specific drugs for other tick-borne flaviviruses associated with severe encephalitis or hemorrhagic fever, underscores the urgent need for progress in understanding the pathogenesis and intervention strategies for TBEV and related flaviviruses. Here we elucidate cellular alterations in the proteome, phosphoproteome, and acetylproteome upon TBEV infection. Our findings reveal a substantial impact of TBEV infection on the innate immune response, ribosomal biogenesis, autophagy, and DNA damage response (DDR). Mechanically, the nonstructural protein NS5 of TBEV impedes DNA damage repair by interacting with SIRT1 to suppress the deacetylation of KAP1 and Ku70. Additionally, the precursor membrane protein prM induces autophagy via associating with AKT1 while constrains autolysosome formation through binding to VPS11. Inhibitors targeting DDR, as well as specific kinases, exhibit potent antiviral activity, suggesting the dysregulated pathways and kinases as potential targets for antiviral intervention. These results from our study contribute to elucidating the pathogenesis and offers insights for developing effective antiviral drugs against TBEV and other tick-borne flaviviruses.

Tick-borne encephalitis virus (TBEV) is an ancient yet often underestimated arbovirus in the *Flaviviridae* family, which include other important medically significant viruses, such as the dengue fever virus (DENV), Zika virus (ZIKV), yellow fever virus (YFV), West Nile virus (WNV), and Japanese encephalitis virus (JEV)[1–4]. TBEV is predominantly transmitted to humans through tick bites and affects the central nervous system, resulting in neurological complications, and in severe cases, leading to fatal outcomes in Europe and Asia[4]. In recent years,

[1]Department of Infectious Diseases and Center of Infectious Diseases and Pathogen Biology, Key Laboratory of Organ Regeneration and Transplantation of the Ministry of Education, State Key Laboratory for Diagnosis and Treatment of Severe Zoonotic Infectious Diseases, The First Hospital of Jilin University, Changchun, China. [2]State Key Laboratory for Diagnosis and Treatment of Severe Zoonotic Infectious Diseases, College of Basic Medical Science, Jilin University, Changchun, China. [3]School of Pharmaceutical Sciences, Jilin University, Changchun, China. [4]Biomaterials and Translational Medicine, Puheng Technology Co., Ltd, Suzhou, China. [5]Clinical Medical College, Changchun University of Chinese Medicine, Changchun, China. [6]China-Japan Union Hospital of Jilin University, Changchun, China. [7]Changchun Veterinary Research Institute, Chinese Academy of Agricultural Sciences, Changchun, China. [8]These authors contributed equally: Liyan Sui, Wenfang Wang. ✉e-mail: yichengzhao@live.cn; qing@jlu.edu.cn; liuquan1973@hotmail.com

there has been an increase in clinical infection reports, along with an expanding geographical distribution of TBEV[5]. Despite the clinical availability of inactivated vaccines, there is currently no specific antiviral drugs for TBEV infections. Furthermore, the emergence of genetic mutations and vaccine-breakthrough infections poses significant challenges to the existing vaccines[6–8]. Additionally, other tick-borne flaviviruses closely related to TBEV, such as Alkhurma hemorrhagic fever virus, Kyasanur forest disease virus, louping ill virus, Omsk haemorrhagic fever virus, and Powassan virus, contribute to severe encephalitis or hemorrhagic fever[9,10]. Unfortunately, no effective vaccines or specific drugs are currently available for these viruses, accentuating the pressing need for advancements in the pathogenesis and intervention strategies.

Like other flaviviruses, TBEV harbors an approximately 11 kb genome encoding three structural proteins, including pre-membrane (prM), envelope (E), and capsid (C), that play crucial roles in virion replication, assembly, and release. Additionally, TBEV possesses seven non-structural proteins (NS1, NS2A, NS2B, NS4, NS4A, NS4B, and NS5), among which NS2B collaborates with NS3 to form the viral protease, while NS5 encodes the methyltransferase and RNA-dependent RNA polymerase (RdRp). Several studies focused on individual viral protein have significantly extended our understanding of the pathophysiology associated with TBEV infection[11–15]. However, the intricate molecular details of the host cells response to TBEV infection remain limited, hindering a comprehensive understanding of potential antiviral targets and countermeasures against tick-borne flaviviruses.

Post-translational modifications (PTMs), including phosphorylation, acetylation, methylation, ubiquitination, glycosylation and succinylation, play important regulatory roles in diverse cellular processes, rendering them appealing targets for antiviral interventions[16,17]. The intricate interplay between different PTMs contributes to the precision and intricacy of cellular regulatory networks. Simultaneous analysis of different PTMs facilitates the examination of the coordinated involvement of regulatory processes during viral infection[18,19]. In this study, we employed an integrated proteomics approach to delineate the cellular responses to TBEV infection across multiple levels, including the proteome, phosphoproteome, and acetylproteome. Our study unveils that TBEV profoundly influences innate immune response, ribosomal biogenesis, autophagy, and DNA damage response (DDR). Specifically, NS5 impedes DNA damage repair and prM induces autophagy. Inhibitors targeting DDR and autophagy, as well as specific kinases, exhibit potent antiviral activity, suggesting the dysregulated pathways and kinases as potential targets for antiviral intervention.

Results

Proteome, phosphoproteome, and acetylproteome analysis upon TBEV infection

In order to unravel host perturbations by TBEV infection, we conducted a comprehensive analysis of proteome, phosphoproteome, and acetylproteome (Figs. 1a–e and S1a–Sc; Supplementary Data 1–6). TBEV infection markedly induced the expression of interferon-stimulated genes (ISGs), including OASL, IFIT1 and IFIT2, as well as pro-inflammatory signals, such as NFKB2 and IL1A (Figs. 1c and S1d; Supplementary Data 1). Furthermore, it upregulated CEBPB, a pivotal transcription factor governing the expression of inflammatory factors, signifying the activation of innate immune response upon TBEV infection (Fig. 1c). Interestingly, TBEV infection also elevated the expression of LRP1, a key entry receptor of Rift Valley fever virus (RVFV), and proteins associated with neurological diseases, such as LLGL1, CNTNAP1, AGRN and SNCA (Figure S1e)[20,21]. Intriguingly, SNCA has been found to play divergent roles, acting as a neuroprotective factor during WNV infection, and as a pathogenic factor in the context of HIV infection[22,23]. Similarly, LLGL1 has been implicated in the asymmetric cell division of neural cells related to microcephaly induced by ZIKV[24]. The precise roles of elevated LRP1, SNCA, and LLGL1 in the pathogenesis of TBEV warrant further investigation. Conversely, TBEV infection resulted in a decreased expression of cell cycle-regulated proteins, including those associated with G2/M transition (CCNB1, AURKB, INCENP, REEP3, UBE2S, PLK1), spindle assembly (KIF11, NEK9, TPX2, KIF22), and cytokinesis (CIT, ANLN, KIF20B) (Fig. 1c). These changes could be linked to the extensive rearrangement of cytoskeletal architecture, implying that TBEV infection may manipulate host cell cycle progression to facilitate virus replication[25].

Our analysis identified 17,300 phosphorylated sites in TBEV-infected cells at 48 h post infection (hpi), with 3,395 phosphorylated sites exhibiting differential expression (Fig. 1b; Supplementary Data 2). To mitigate the influence of unmodified proteins, we compared the fold-changes of phosphorylated sites to protein abundance (Fig. 1d; Supplementary Data 3). TBEV infection affected the phosphorylation of several effector proteins involved in cytoskeleton organization (MAP1B, VIM, TJP1 and MACF1), DNA damage response (PRKDC, BOD1L1, TP53BP1 and XRCC1), as well as the autophagy receptors (NBR1 and SQSTM1) (Fig. 1d). Additionally, we noted alterations in the phosphorylation status of neural differentiation factors, including CUX1 and AHNAK. Notably, influenza A virus (IAV) infection also modulates AHNAK phosphorylation, and AHNAK plays beneficial roles for the replication of both IAV and SARS-CoV-2[26]. The restriction factor SAMHD1 exhibited reduced phosphorylation levels at S18, S33 and S278 upon TBEV infection, a phenomenon also seen during HIV and human cytomegalovirus (HCMV) infection[27,28].

The regulation of known phosphorylated sites hints at the involvement of kinases in the control of essential cellular processes[29]. We found diminished activity of cell cycle-related kinases (CDK1, CDK2, CDK5, CDK9, WEE1) and mitogen-activated protein kinases (MAPK1/3/8, MAPK2K4/5/6). Conversely, an expected increase in the activity of kinases associated with cell proliferation and motility (PIM1, PRKD1/2), DNA damage response (ATM, ATR, PRKDC), PRKG1/2, and CLK1/2 was observed (Fig. 1f; Supplementary Data 4 and 5). Consistent with TBEV, ZIKV infection also increases the phosphorylation of ATR and PRKDC substrates[30], suggestive of the conserved regulation of host DNA damage response by flaviviruses. As TBEV infection can induce endoplasmic reticulum (ER) stress[31], we also found that TBEV infection obviously activated the phosphorylation of PERK at 12 hpi, while EIF-2α was obviously phosphorylated at 24 hpi, further confirming the activated ER stress upon TBEV infection (Figure S2a).

Among the 7063 acetylated sites we identified, 1756 acetylated sites exhibited significant changes, with most proteins demonstrating hyperacetylation upon TBEV infection (Figs. 1b and S1f; Supplementary Data 3 and 6). Notably, TBEV induced specific acetylation pattern in mitochondrial metabolism enzymes (ACLY, ACSF2, GOT2, HMGCL and MTHFD2), and proteins responsible for RNA splicing and processing (DDX17, NCL, TRMT10C, HNRNPU and YTHDF3) (Fig. 1e). Particularly intriguing is the acetylation of histones, including H1.4, H1.5, H2BC3 and H4-16, which are associated with chromatin condensation and accessibility[32]. Strikingly, TBEV infection led to a noticeable decrease in histone acetylation, suggesting that TBEV may affect the transcriptional activity of host cells by concurrently managing histone acetylation. Additionally, TBEV infection increased the acetylation of acetyltransferase HAT1 and EP300, in theory, the acetylation degree should be positively correlated with their enzymatic activity[33,34]. This may account for the heightened acetylation observed in host proteins upon TBEV infection.

We further screened the significantly altered acetylation sites and identified 59 sites that exhibited clear changes at both 6, 12, 24, and 48 hpi (Figure S2b). Notably, these sites displayed a consistent increase in acetylation, aligning with the overall rise in acetylation levels following TBEV infection. Among these sites, the innate immune regulator STAT1 showed a pronounced increase in acetylation, which may be associated with the activation of innate immunity in response to TBEV.

Additionally, ER-resident proteins, such as CANX and HSPA5, displayed noticeable acetylation, potentially linked to TBEV-induced ER stress. Furthermore, the receptor of arenaviruses[35], TFRC, exhibited elevated acetylation at the K399 site, which may be related to TBEV replication.

Our analysis uncovered a complex interplay between phosphorylation and acetylation patterns in response to TBEV infection. UHRF1, for instance, exhibited simultaneous phosphorylation at S178 and S302, accompanied with elevated acetylation at K577. Interestingly, there was a substantial decrease in the protein level of UHRF1 following TBEV infection, possible due to phosphorylation-induced instability of UHRF1 (Fig. 1c–e)[36]. We further found that the overexpression of UHRF1 significantly suppressed TBEV replication, as evidenced by results from PCR, immunoblotting (IB), and $TCID_{50}$ assays (Fig. S2c–e). A similar downregulation of UHRF1 has been observed in herpes simplex virus-1 (HSV-1) infected cells, where it is believed to inhibit HSV-1 replication by inducing interferon production[37], suggesting that UHRF1 may serve as a restriction factor across different types of viruses. In contrast, AHNAK displayed acetylation modifications primarily concentrated at the N-terminal, while the C-terminal underwent more frequently phosphorylation events (Figure S2f, g). These findings underscore the importance of simultaneously investigating various post-translational modifications that may reshape the functions of targeted proteins during virus infection.

Post-translational modification of viral proteins

PTMs of viral proteins may profoundly affect virus entry, replication, assembly, and release[38,39]. We observed phosphorylation of four TBEV proteins, namely prM, NS2B, NS3, and NS5 (Figure S3a–c; Supplementary Data 7). Notably, NS5 exhibited 15 phosphorylation sites, with the S602, T612, S848 and S849 being conserved among different flaviviruses (Figure S4a). Interestingly, S602 shared a conserved site with HCV NS5 (S282), which can be phosphorylated by AKT, thereby regulating the polymerase activity of NS5 and influencing viral replication[40,41]. Conversely, the five phosphorylation sites on NS3 were

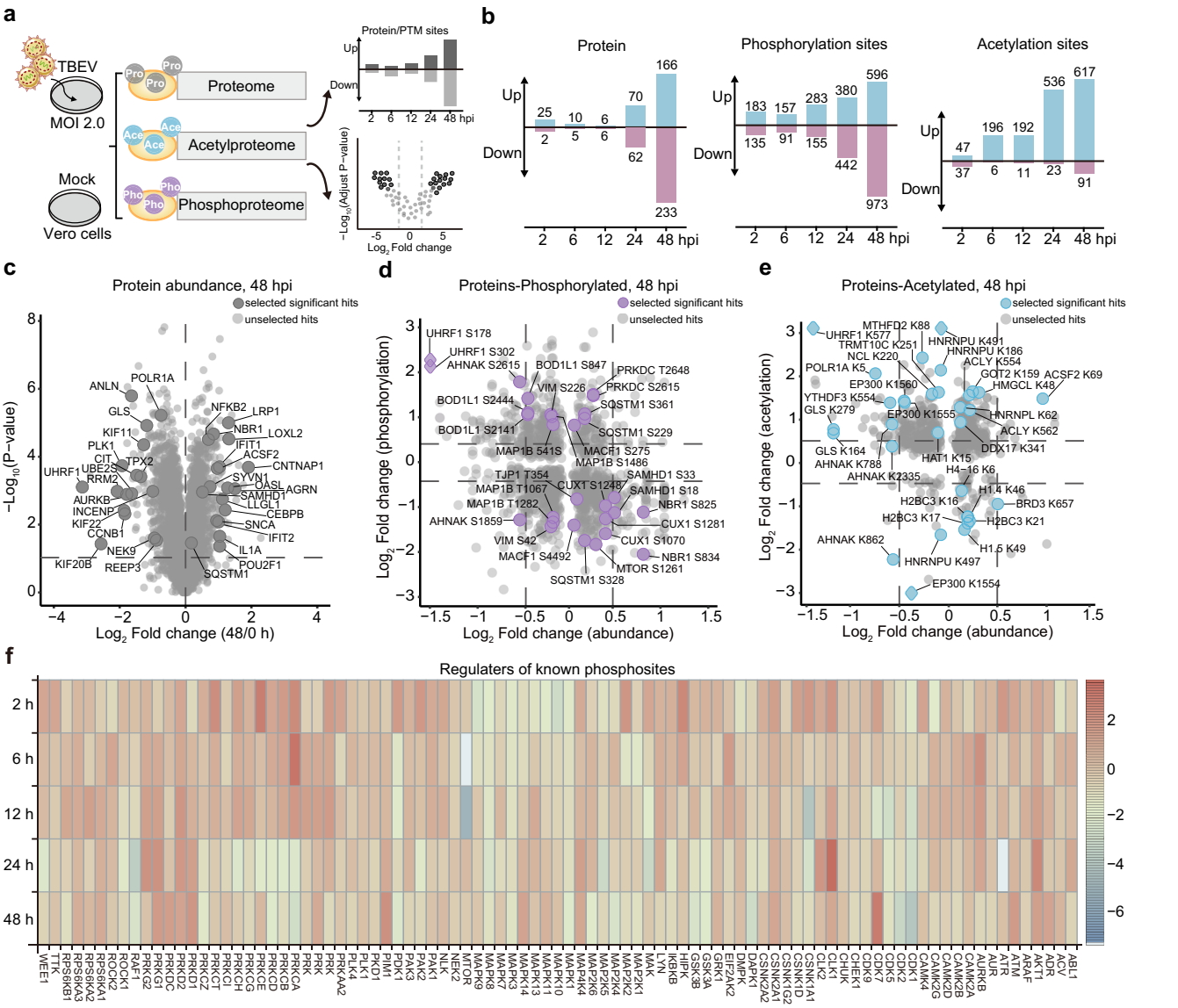

Fig. 1 | Proteome, phosphoproteome and acetylproteome analysis upon TBEV infection. a Vero cells infected with TBEV were collected at 2, 6, 12, 24, and 48 hpi. The cells were lysed and digested into peptides for quantitative proteomics, phosphoproteomics, and acetylproteomics analyses. hpi, hours post-infection. **b** The number of unique proteins, phosphorylation and acetylation sites exhibiting significant up(blue) or downregulation (purple) at specific time points following TBEV infection (| Log_2FC | > 1.5, *P* value < 0.05). **c** Volcano plot of protein abundance at 48 hpi compared to the mock-infected cells. **d**, **e** Comparison of phosphorylated (**d**) and acetylated sites (**e**) with protein abundance at 48 hpi. **f** Kinases displaying significant changes in activity upon TBEV infection. Statistical significance in b and c was assessed using the two-sided Student's t-test to determine *P* values.

exclusively conserved among tick-borne flaviviruses, indicating a unique function of NS3 phosphorylation for tick-borne flaviviruses (Figure S4b).

Of the ten TBEV proteins, seven proteins underwent acetylation, with E, NS3 and NS5 being the most heavily modified viral proteins (Figure S3d–f). The E protein, for instance, displayed six acetylated sites, all within the non-cytoplasmic domain. It's worth noting that the ubiquitination within the non-cytoplasmic domain of ZIKV E protein is a crucial determinant for virus entry and pathogenesis, underscoring the pivotal role of modifications within non-cytoplasmic domain of E protein[39]. Furthermore, the nine extensive acetylation events on NS5 protein were distributed across both N-terminal methylation domain and C-terminal RdRp domain. Among these, K182, K402, K686 and K841 were conserved among different flaviviruses (Figure S4a). Notably, the RdRp domain of NS5 is essential for binding to stem-loop A (SLA) of the RNA genome and initiating RNA synthesis. K182, located in the N-terminal region of NS5, plays a pivotal role in methyltransferase activity. K841 is recognized as a critical binding site for SLA in flavivirus NS5[42]. These findings show the critical regulatory functions of acetylation on TBEV NS5. Mapping these sites onto the atomic structure of NS3 and NS5 highlights their critical positions for the function of these proteins (Fig. S3g–j). Collectively, the identification of TBEV-specific modified sites reveals viral protein-specific functions, while the conserved post-translational modifications hold the potential to develop broad-spectrum antiviral drugs against flaviviruses.

Multi-proteomics analysis reveals key pathways in response to TBEV infection

To investigate the integrated regulation of protein abundance, phosphorylation, and acetylation, we conducted an enrichment analysis, with a particular focus on phosphorylated and acetylated sites and their associated proteins. Our findings showed that downregulated proteins and phosphorylated proteins were primarily pertained to the regulation of cell cycle, including the G1/S transition, G2/M transition, and the mitotic cell cycle (Figure S5a; Supplementary Data 8). Conversely, elevated acetylation was predominantly associated with the metabolism of amino acids and mRNA. The upregulated phosphorylated proteins played crucial roles in fundamental cellular processes, including ribosomal biogenesis and processing, cellular responses to DNA damage stimuli, and subsequent double-strand break repair via the nonhomologous end joining (NHEJ) pathway (Figure S5a).

We concentrated on the perturbed signaling pathways characterized by both aberrant protein levels and modifications, such as ribosomal biogenesis and DNA damage response, together with the conventional signaling pathways that closely linked to virus infection, including inflammatory response and autophagy, and delineated the disruption of these pathways by TBEV infection (Fig. 2a). To understand the possible mechanism of perturbed pathways by TBEV, we predicted the interactions between host proteins and viral proteins (Figure S5b)[13,43,44]. Our analysis revealed the modulation of innate immune response and autophagy by NS2B3 and prM, along with the disturbed ribosomal biogenesis and DNA damage response (DDR) by NS5 (Fig. 2b).

The induction of ISGs at the proteome level can be attributed to the upregulated DDX58 (RIG-I) and TLR3, suggestive of host innate immune response to TBEV infection (Figs. 1c and 2b). However, viruses often exploit key cellular components to dampen innate immune response and survive within host cells. In this context, prM and NS2B3 were shown to antagonize type I interferon production by interacting with MAVS and UNC93B1, respectively (Fig. 2b).

Viruses often manipulate autophagy to enhance their replication[45]. Our study indicated that prM and NS1 could participate in the modulation of autophagy induction. Furthermore, prM and NS2B3 were predicted to regulate the formation of autolysosome, leading to the accumulation of autophagic receptors NBR1 and OPTN (Figs. 2b and S6a). Disruption of autolysosome formation can directly affect protein degradation processes. Notably, we observed a significant increase in the expression of SNCA following TBEV infection, a protein that undergoes degradation through autophagy (Figs. 1c, S1e and S6a)[46]. The aggregation of SNCA is a hallmark of Parkinson's disease, suggesting its potential involvement in TBEV-induced neuronal diseases[47].

We observed significant regulated ribosomal biogenesis as a consequence of TBEV infection (Figs. S5a and 2b), with the analysis revealed a connection between NS5 and the 90S pre-ribosome components (UTP20), which may explain the reduced synthesis of rRNA and its precursor due to TBEV infection[48]. TBEV infection was also shown to play a role in the regulation of DDR, as NS5 was implicated in its interactions or modulation of the acetylation and phosphorylation levels of key factors associated with damage repair (Figs. 2b, S6b, c).

NS5 interferes with host DNA damage response through interacting with SIRT1

Given the strong indications of DDR involvement during TBEV infection (Figs. 2b and S5a), we set out to investigate the specific impact of TBEV infection on DDR and explore the underlying mechanisms. DNA single-strand and double-strand breaks (SSBs and DSBs) can activate ataxia telangiectasia and Rad3-related (ATR) or ataxia-telangiectasia mutated (ATM), which undergo autophosphorylation and consequently phosphorylate downstream factors to activate DNA damage response[49].

The analysis of kinase activity revealed the activation of ATM, ATR and DNA-PK (a kinase involved in DNA repair) at 48 hpi upon TBEV infection (Fig. 1f). This activation was evident from the significantly increased phosphorylation of several substrates of ATM (KAP1, Ku70 and HNRNPA1), ATR (NPM1 and NUP107) and DNA-PK (XRCC1 and HNRNPA1) (Figure S6b; Supplementary Data 4). TBEV infection also induced the direct phosphorylation of DNA-PK at S2615, indicating the activation of DDR by virus infection (Figure S6b).

We further examined the engagement of DDR signaling at 24 and 48 hpi, using hydroxyurea (HU), a substance known to induce DNA replication stress and activate ATR, as a positive control. A549 cells, which are human origin that sensitive to TBEV infection, was used in our following analysis[50]. Consistent with the kinase activity analysis and phosphor-proteomic results, TBEV infection significantly enhanced the phosphorylation of DNA-PK (pDNA-PK^{S2056}), ATR (pATR^{T1989}), ATM (pATM^{S1981}), CHK1 (pCHK1^{S317}), CHK2 (pCHK2^{T68}), and KAP1 (pKAP1^{S824}), along with phosphorylated H2AX (γH2AX), a hallmark of DSB (Fig. 3a, b). To confirm the impact of TBEV on DDR at the single-cell resolution, immunofluorescence analysis revealed an increased number of pKAP1^{S824}, pCHK1^{S317} and γH2A.X foci per TBEV-infected cell compared with uninfected cell (Figure S7a–f). Additionally, the comet assay demonstrated the induction of DNA fragmentation by TBEV (Fig. 3c, d). These results collectively indicate that TBEV infection induces DNA damage. Activation of DDR has been associated with cellular senescence, inflammation, and cell cycle arrest[51,52]. Notably, TBEV infection significantly elevated the expression of *NFKB, IL1A, IL6, IL8* and *CXCL10* at 24 and 48 h post TBEV infection (Figures S8a,b). Together with the increased senescence-associated β-galactosidase (SA-β-gal) activity, the heightened abundance of P21 but reduced the expression of MKI67 (Figure S8c–g), indicating the induction of cellular senescence and proinflammation upon TBEV infection, respectively. Concurrently, our analysis regarding the impact of TBEV on cell cycle prompted an investigation into its effect on cell cycle progression, revealing a noticeable increase in the percentage of cells in G0/G1 phase, suggesting the influence of TBEV on cell cycle progression without inducing apoptosis (Figure S8h–l).

Following the detection of DNA damage, the deployment of DNA repair proteins depends on the type of lesions encountered. During the G1 phase, the accumulation in 53BP1 at the break promotes repair through NHEJ[53]. Notably, we observed a pronounced reduction of

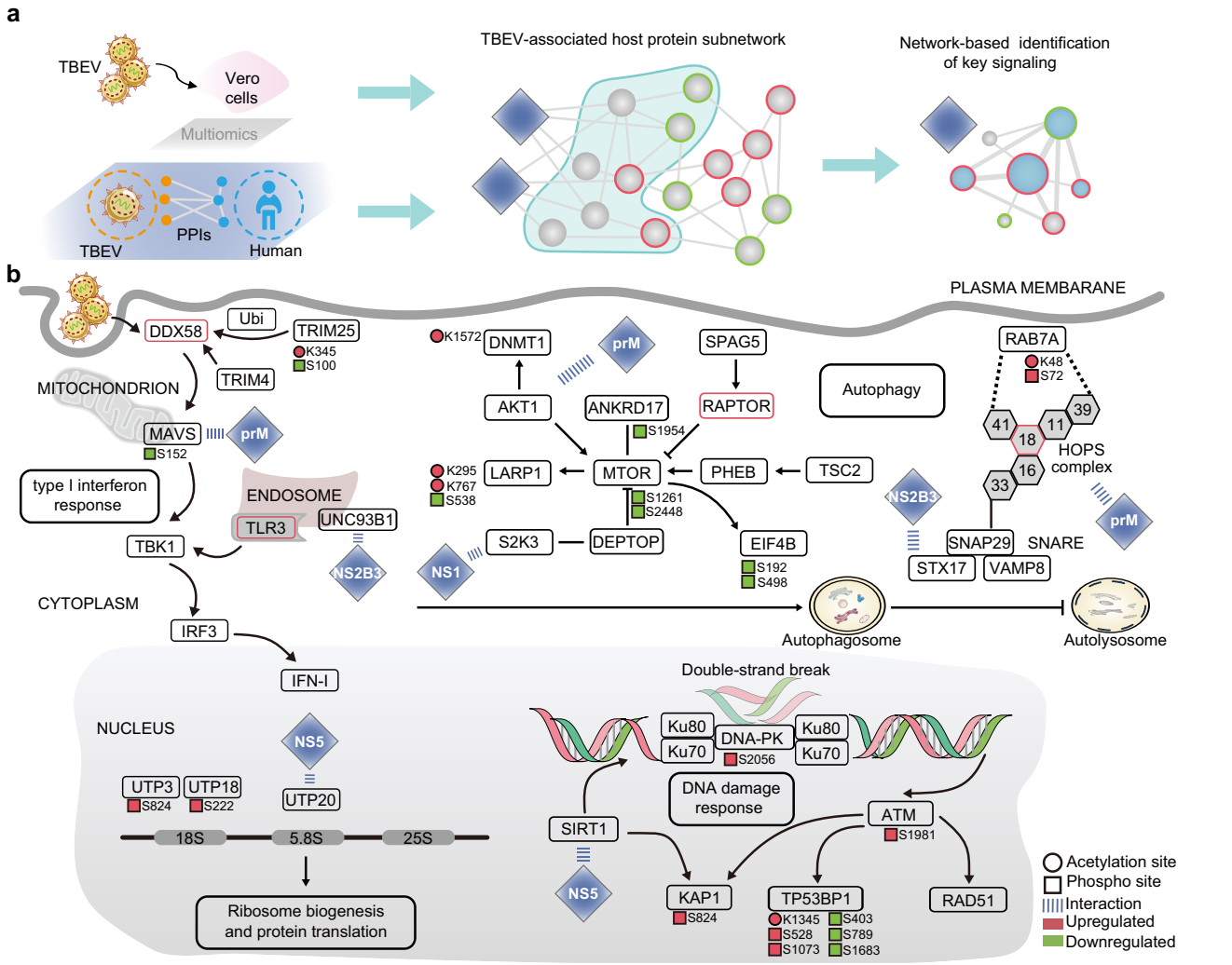

Fig. 2 | Multi-omics analysis reveals molecular pathways perturbed by TBEV infection. a Multi-proteomics analysis identified host cellular pathways perturbed by TBEV infection. **b** Predicted correlation of TBEV proteins with type I interferon response, ribosomal biogenesis, autophagy, and DNA damage response.

53BP1 foci in TBEV-infected cells, and the accumulation of γH2A.X foci was not accompanied with the 53BP1 foci accumulation (Figure S9a–c). Consistently, we also observed the increased accumulation of γH2A.X foci and decreased 53BP1 foci in TBEV-infected mice, suggesting the activation of DNA damage and a diminished efficiency of NHEJ upon TBEV infection (Figure S9d–g). XRCC5/6 (Ku80/70) and DNA-PK function as core proteins of NHEJ[54]. While the expression of Ku70/80 and DNA-PK showed no apparent changes after TBEV infection, we detected alteration in the phosphorylation and acetylation of NHEJ factors. Specifically, the phosphorylation of DNA-PK and Ku70 was significantly elevated upon TBEV infection, although the phosphorylation of Ku70 has been found not to be directly related to its function in NHEJ[55]. Conversely, acetylproteomics indicated a significant increase in the acetylation of Ku70 (K556 and K605), Ku80 (K144), DNA-PK (K703 and K2224) and KAP1 (K337) upon TBEV infection (Figure S6c). Acetylation of KAP1 and Ku70, known to be regulated by SIRT1, has been found to play a role in regulating DNA repair activity[56,57]. Considering the interaction between TBEV NS5 and SIRT1 (Fig. 2b), and the observed reduction in 53BP1 foci in NS5-overexpressed cells (Figure S7g, h), we hypothesized that NS5 might engage with SIRT1 and inhibit SIRT1-mediated deacetylation of Ku70 and KAP1, consequently suppressing the efficiency of NHEJ activity.

Co-immunoprecipitation demonstrated the binding capacity of both overexpressed and endogenous SIRT1 to NS5, the MTase domain of NS5 mainly responsible for the interaction with SIRT1. Additionally, the co-localization of NS5 and SIRT1 was observed in the nucleus through immunofluorescence assay (Figs. 3e, S9h–k). In accordance with previous findings, our study validated that the interaction of SIRT1 with both Ku70 and KAP1, while no binding was observed with Ku80 or DNA-PK (Figs. 3f and S9l). Notably, overexpression of SIRT1 led to a reduction in the acetylation levels of Ku70 and KAP1 (Figure S9m). Conversely, the overexpression of NS5 or TBEV infection resulted in a significant elevation of acetylation levels, as determined by co-immunoprecipitation using both anti-pan acetylation and Ku70 antibodies (Figs. 3g–j and S9n–p). Furthermore, we observed a decrease in the acetylation of Ku80 upon SIRT1 overexpression and an increase in acetylation after NS5 expression or TBEV infection (Figs. 3g–j and S9n–p). Given the absence of direct interaction between SIRT1 and Ku80, the modulation of Ku80 acetylation may be governed by an indirect pathway associated with SIRT1. Considering the regulatory role of acetylation status of Ku70 and KAP1 on NHEJ activity, we thus assessed the impact of NS5 overexpression on NHEJ efficiency using ISec-I based EJ5-GFP reporter assay, revealing a significant decrease in NHEJ-mediated DSB repair compared with control cells (Fig. 3k). Additionally, the accumulation of 53BP1 foci was reduced upon NS5 overexpression (Figure S7g, h). Consistently, TBEV infection also decreased NHEJ activity, as assessed by EJ5-GFP reporter assay (Fig. 3k).

https://doi.org/10.1038/s41467-024-54628-w

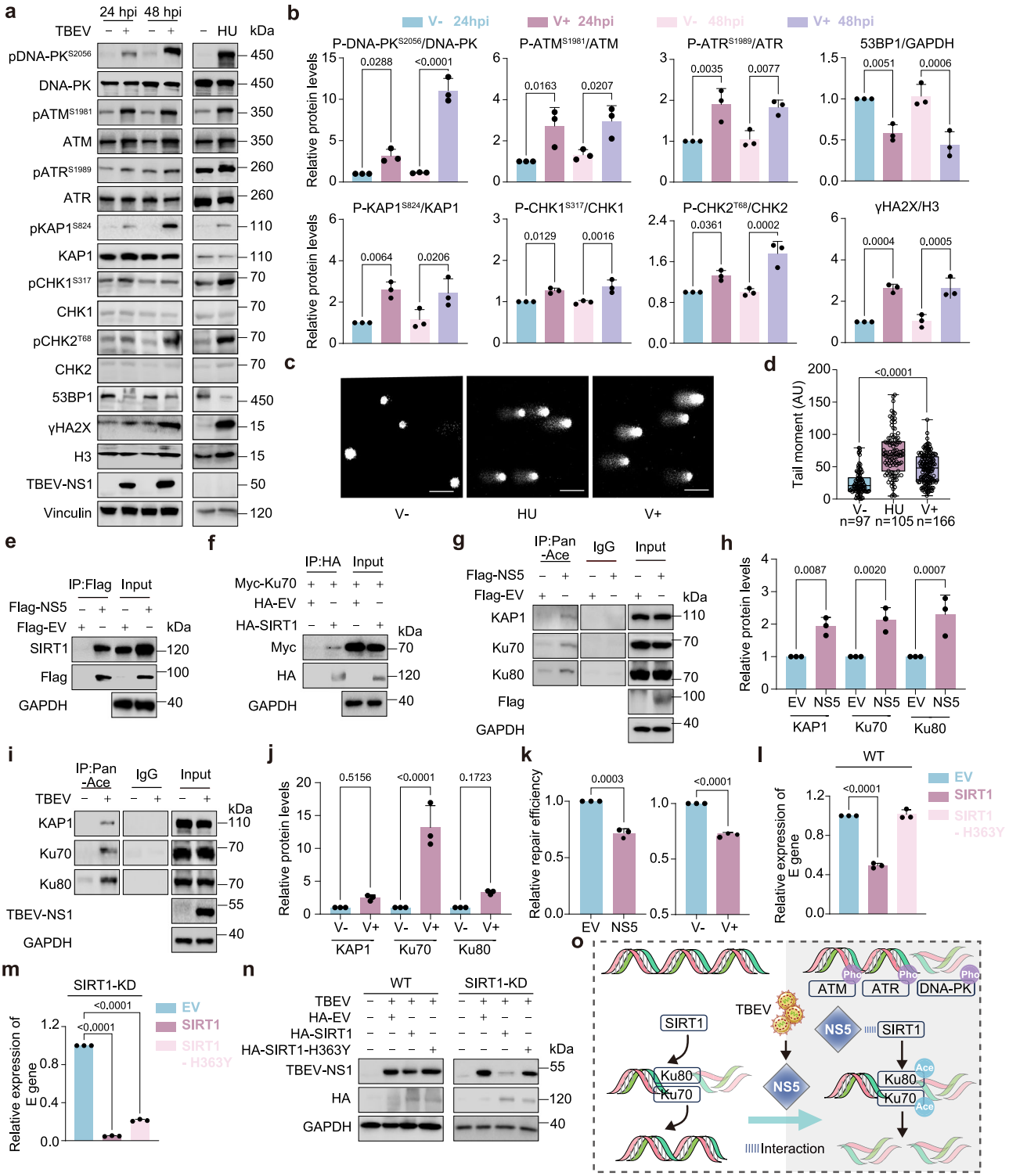

Having established that NS5 can modulate SIRT1 to regulate DNA repair processes, we explored the role of SIRT1 in the context of viral replication. Our results demonstrated that overexpression of SIRT1 significantly inhibited TBEV replication, while knockdown of SIRT1 had no significant effect on viral proliferation (Figure S10a–d). Given that the catalytic domain of SIRT1 is essential for deacetylating Ku70, we further constructed a plasmid expressing SIRT1-H363Y (catalytically inactive form of SIRT1). Consistently, the overexpression of WT SIRT1 in SIRT1 KD cells led to a significant reduction in the mRNA and protein abundance of TBEV, while the introduction of SIRT1-H363Y did not have a significant impact on viral proliferation compared with control group (Figs. 3l–n and S10e). Furthermore, the deacetylation mutation of Ku70 (K556R) showed obviously inhibition on the transcription of TBEV (Figure S10f). Taken together, TBEV NS5 binds to and suppresses the activity of SIRT1, resulting in the elevated acetylation of Ku70 and KAP1, which in turn inhibits DNA damage repairment and promotes virus replication (Fig. 3o).

prM induces autophagy but inhibits the formation of autolysosome

Based on the analysis that TBEV may modulate autophagy (Fig. 2b), we further confirmed the effect of TBEV on autophagy and elucidated the

Fig. 3 | NS5 interferes with host DDR through interacting with SIRT1. **a** Immunoblot assays showing increased levels of proteins associated with DNA damage and altered DDR activation in TBEV-infected cells. A549 cells were infected with TBEV and harvested at 24 and 48 hpi. Lane 2 and lane 4 show cells infected at 24 and 48 hpi at MOI 2.0, respectively. Lane 5 and lane 6 show lysates from A549 cells not treated (-) or treated with 6 mM HU as positive controls. Proteins levels associated with DNA damage and altered DDR activation are normalized by vinculin and set to 1.00 in control cells. **b** Quantification of activated protein levels shown in (**a**) values normalized to mock-infected samples. **c** Images of comet assays from mock or TBEV-infected cells at 24 hpi. Scale bar, 20 μm. **d** Quantification of comet tail moment shown in (**c**). **e** Co-precipitation of endogenous (*left*) and overexpressed SIRT1 (*right*) by Flag-NS5 in coimmunoprecipitation assay. Data representative of three independent experiments with similar results. **f** Co-precipitation of overexpressed Myc-Ku70 by HA-SIRT1 analyzed by coimmunoprecipitation assay. Data representative of three independent experiments with similar results. **g**–**j** Higher levels of endogenous KAP1, Ku70 and Ku80 precipitated by anti-pan acetylation antibody in NS5 overexpressed (**g**) and TBEV-infected (**i**) cells compared to control cells. Quantification of acetylated KAP1, Ku70 and Ku80 in NS5 overexpressed (**h**) and TBEV-infected (**j**) cells. **k** Evaluation of DSB re-joining in EJ5-GFP HEK293T cells transfected with I-SceI together with Flag-EV or Flag-NS5 (*left*) or mock-infected cells or cells infected with TBEV (*right*). **l**–**n** Overexpression of SIRT1 but not SIRT1-H363Y suppressed levels of E genes (**l** and **m**) and TBEV-NS1 protein (**n**) in WT and SIRT1-KD cells. Cells transfected with SIRT1 or SIRT1-H363Y were infected with TEBV, TBEV-NS1 protein was analyzed by immunoblot assay. **o** Subnetworks revealing associations between TBEV and host targets and factors implicated in the modulation of DNA damage. Each point represents a sample. Data are represented as mean ± SEM of 3 independent experiments. The *P*-values are calculated and reported using one-way ANOVA (**b**, **h**, **j**–**m**). For all boxplots (**d**), median, upper and lower quartile as well as significance levels of *P* values from two-sided Wilcoxon test are shown. Detailed information of each sample is provided as a Source Data file.

underlying mechanisms. Our initial examination revealed that TBEV infection increased the conversion of the light chain 3 (LC3)-I to LC3-II (Figure S11a, b). We also observed a noticeable accumulation of punctate GFP-LC3 in TBEV infected cells compared with mock-infected cells (Figure S11c, d). Transmission electron microscopy (TEM) analysis further confirmed a higher abundance of double-membrane autophagosomes during TBEV infection, providing strong evidence that TBEV infection induces autophagy (Figure S11e). Consistent with proteomic data, the expression level of P62 (SQSTM1), another autophagic marker, showed a slight increase, suggesting a potential blockage of autophagic flux (Figs. 1c, S11a, b). To examine autophagic flux, we utilized RFP-GFP-LC3, a dual-fluorescence reporter. In acidic lysosomal environments, GFP fluorescence is quenched while RFP fluorescence persists[58]. Notably, a significantly higher yellow puncta per cell was observed in TBEV infected cells compared with mock-infected cells, indicating TBEV infection blocked the formation of acidified autolysosomes (Figures S11f, g).

Our investigation into the effects of TBEV proteins on autophagy revealed that prM and NS2B3 were closely associated with autophagy regulation. Notably, prM induced a more robust accumulation of GFP-LC3 puncta compared to NS2B3 (Figure S12a). Autophagy initiation is tightly regulated by the AKT-mTOR signaling pathway, which is often manipulated by RNA viruses to induce autophagy[59,60]. Our analysis showed the interaction between prM and AKT1, and a significant decrease in mTOR phosphorylation (Figs. 1d and 2b), suggesting a possible link between prM and autophagy induction mediated by the AKT1-mTOR pathway. We confirmed the interaction of prM and AKT1 using co-immunoprecipitation and observed co-localization of AKT1 and prM in the cytoplasm (Fig. 4a, b). Overexpression of prM led to the suppression of AKT1 phosphorylation at both S473 and T308, subsequently reducing mTOR phosphorylation at S2448 (Fig. 4c, d). Consistent with the observations in TBEV-infected cells, prM overexpression increased P62 levels, the LC3-II/LC3-I ratio, and induced the accumulation of GFP-LC3 puncta, confirming that prM indeed induced the formation of autophagosomes (Fig. 4e–h). We further detected whether TBEV infection also suppressed AKT1-mTOR signaling, and found that TBEV infection reduced mTOR phosphorylation. Additionally, the phosphorylation of AKT1 significantly increased at 1 hpi, but decreased notably at 24 and 48 hpi, suggesting that the reduced AKT1-mTOR signaling in response to viral infection might be linked to autophagy induction (Figure S11h, i). To further explore the effect of suppressed AKT1 on TBEV infection, we overexpressed AKT1 and found that AKT1 overexpression significantly suppressed TBEV replication (Fig. 4i–k).

The increased P62 levels observed after prM overexpression indicated that the autophagic flux might be blocked. To assess changes in autophagic flux following prM overexpression, we utilized GFP-RFP-LC3 to detect the autophagosome formation and lysosomal fusion. Results revealed an obvious accumulation of yellow LC3 puncta in prM-overexpressed cells, indicating a blockade in autophagic flux (Figure S12b, c). Additionally, the colocalization of LC3-labeled autophagosome and LAMP1-labeled lysosomes was disrupted in prM-overexpressed cells, suggesting that prM inhibited the formation of autolysosome (Figure S12d). prM was predicted to interact with VPS11, a component of the HOPS complex, which plays a crucial role in autophagic flux[61,62]. Further experiment indicated that PrM could co-precipitated and colocalized with VPS11 (Figs. 4l and S12e), and the interaction between VPS11 and VPS18/VPS41 was disrupted in prM-expression cells, indicating an interference with HOPS complex formation by prM (Fig. 4m).

After observing the interaction of NS2B3 and STX17 (Fig. S5b), a key regulator of autophagic flux, we proceeded to assess autophagic flux following NS2B3 overexpression. Our results revealed that NS2B3 induced a higher number of $GFP^{-}RFP^{+}$LC3 foci compared to the control under starvation conditions (Figure S12f). Co-immunoprecipitation analysis confirmed the interaction between NS2B3 and STX17, with both proteins colocalizing in the cytoplasm (Figure S12g, h). Furthermore, NS2B3 overexpression led to an increase in LC3-II levels and a decrease in P62 expression, indicating that NS2B3 promotes autophagic flux (Figure S12i).

To demonstrate the role of autophagy during TBEV infection, we specifically knocked down ATG7 using small interfering RNA (siRNA). This resulted in a significant decrease in TBEV mRNA and protein levels, as well as reduced viral titers compared to cells transfected with non-targeted control siRNA (siNC) (Fig. 4n–q). Taken together, prM interacts with AKT1 to induce autophagy. Concurrently, prM and NS2B3 interact with VPS11 and STX17 respectively to modulate the formation of autolysosome (Fig. 4r).

TBEV infection regulates the DNA damage response and autophagy in neuronal cells and brain organoids

Given the sensitivity of neuronal cells to TBEV infection and the adverse effects associated with it, we sought to investigate the impact of TBEV on both neuronal cells and brain organoids (Fig. 5a). For our analysis of DNA damage and autophagy, we selected T98G, a human brain glioma cell line recognized for its susceptibility to TBEV infection. Our results demonstrated that TBEV infection significantly induced the accumulation of γH2A.X (Fig. 5b, c). Additionally, the comet assay conducted on TBEV-infected neuronal cells provided further evidence of DNA fragmentation resulting from the infection (Fig. 5d, e). Moreover, our analysis revealed that TBEV infection resulted in an increased LC3-II/LC3-I ratio, while P62 levels remained unchanged in TBEV-infected T98G cells (Fig. 5f, g). Notably, we observed a pronounced accumulation of GFP^{+}LC3 foci and a higher percentage of yellow foci in TBEV-infected T98G cells compared to mock-infected controls (Figs. 5h, i, S13a, b). These findings further

https://doi.org/10.1038/s41467-024-54628-w

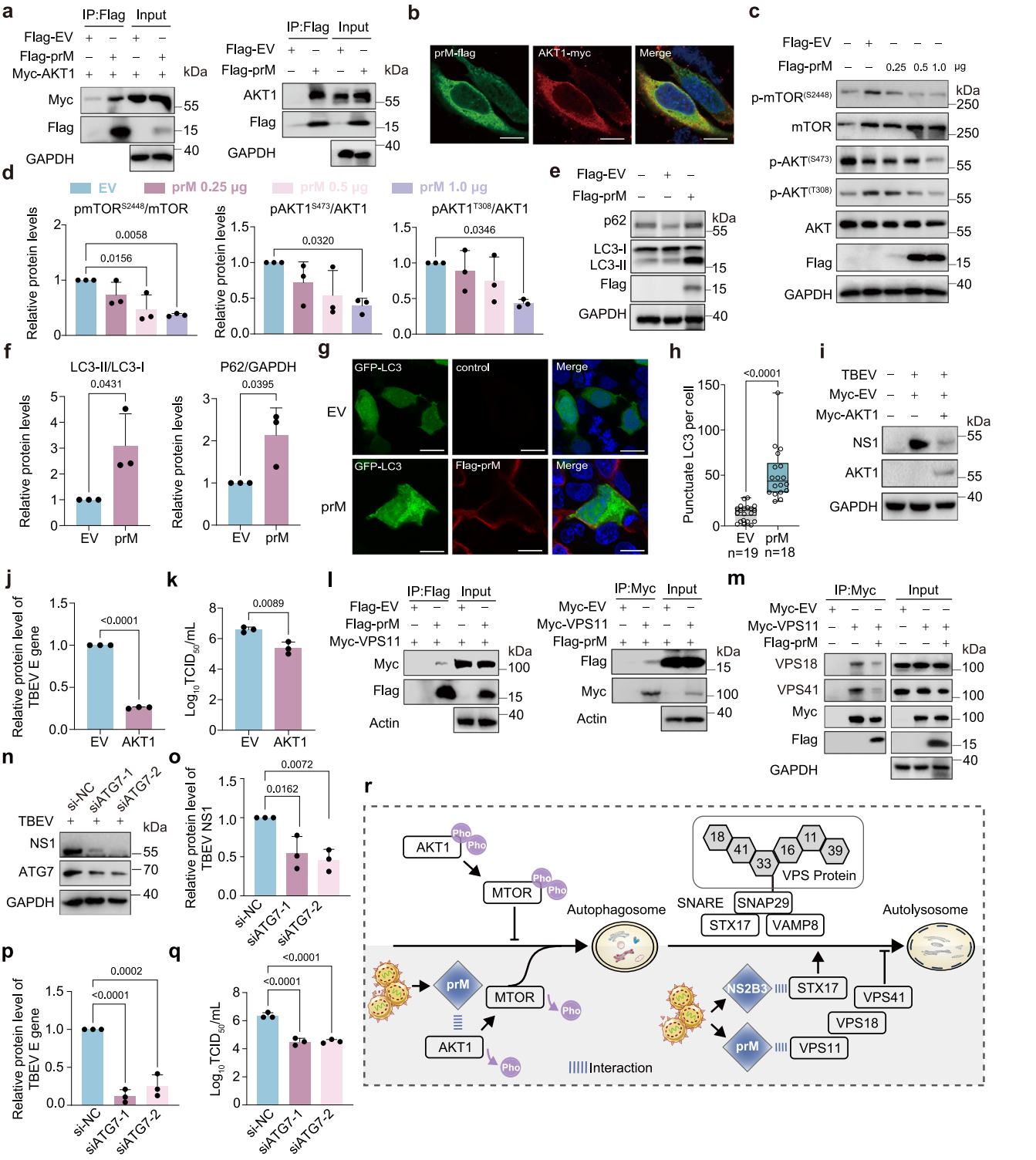

support the hypothesis that TBEV infection induces autophagy while concurrently inhibiting autophagic flux in neuro cells.

Brain organoid generated from induced pluripotent stem cells serves as an excellent model for studying neurotropic viruses and the associated neuronal damage. To further elucidate the effects of TBEV on DDR and autophagy, we utilized TBEV-infected brain organoids. Characterization of the brain organoid confirmed the presence of neural progenitor (SOX2), oligodendrocyte (Oligo2), immature neurons (TUJ1), and mature neuronal (NeuN) markers (Figures S13c, d). A gradual increase in viral titer throughout the infection period confirmed successful infection of TBEV, which primarily localized in mature neuronal cells and astrocytes (Figures S13e, f). Concurrently, we observed a significant increase in the intensity of γH2AX in TBEV-infected organoid compared to the mock-infected group, as indicated by both immunoblot and immunofluorescence staining assays (Fig. 5j–m). These findings suggest the activation of DNA damage in response to TBEV infection. Conversely, we noted a reduction in the number of 53BP1 foci following TBEV infection, implying a reduction in the repairment of DNA damage (Fig. 5n, o). Furthermore, our analysis of TBEV-infected brain organoids revealed elevated LC-II/LC3-I ratios and P62 levels, along with an increased abundance of LC3 puncta, supporting the conclusion that TBEV infection induces autophagy

Fig. 4 | PrM induces autophagy but inhibits the formation of autolysosome. **a** Co-immunoprecipitation demonstrating the interaction between prM and over-expressed (*left*) and endogenous (*right*) AKT1 in Flag-tagged empty vector (EV) or prM and Myc-tagged AKT1 in HEK293T cells. **b** Immunofluorescence analysis showing the co-localization of prM and AKT1 in the cytoplasm. Scale bar, 10 μm. **c** Immunoblot assay showing decreased phosphorylated AKT1 (S473 and T308) and mTOR (S2448) in cells expressing various amounts of TBEV prM. **d** Quantification of decreased phorsphorylated proteins in (**c**). **e** Immunoblot assay showing that increased expression of LC3 and P62 in prM overexpressed cells. **f** Quantification of increased percentage of LC3-II/LC3-I and p62/GAPDH in (**e**). **g** Cells expressing prM contained more GFP$^+$LC3 puncta compared with EV transfected cells. Scale bar, 10 μm. **h** Quantification of the number of GFP$^+$ LC3 puncta per cell in (**g**). **i** Immunoblot assay showing that AKT1 overexpression leads to a reduction in TBEV NS1 protein. **j** Quantification of decreased protein level of NS1 in (**i**). **k** Viral titers in supernatants significantly decreased in cells transfected with Myc-AKT1 compared to cells transfected with empty vector. **l** Co-immunoprecipitation demonstrating interaction of prM and VPS11 in Flag-prM and Myc-VPS11 overexpressed cells. **m** Co-precipitation showing a reduction in VPS18 and VPS41 co-precipitated by VPS11 in cells overexpressed with prM compared with empty vector transfected cells. **n** Immunoblot assay demonstrating a significant reduction in TBEV NS1 protein levels in ATsiRNA-1 (si1) and siRNA-2 (si2) transfected cells compared to cells transfected with siNC (non-targeted control siRNA). **o** Quantification of the protein level of TBEV NS1 in (**n**). **p**, **q** In cells transfected with ATG7 si1 and si2, E genes (**p**) and viral titers (**q**) in supernatants significantly decreased compared to cells transfected with si-NC. **r** Outline of host-cell autophagy regulated by TBEV prM and NS2B3. Data prensted in (**a**, **b**, **l**, **m**, and **n**) are representative of three independent experiments with similar results. Each point represents a sample. Data are represented as mean ± SEM of 3 independent experiments. The *P*-values are calculated and reported using one-way ANOVA (**d**, **f**, **j**, **k**, **o**, **p**, **q**). For boxplots (**h**), median, upper and lower quartile as well as significance levels of *P* values from two-sided Wilcoxon test are shown. Source data are provided as a Source Data file.

(Fig. 5p, q). These findings provide further evidence of the regulated DDR and autophagy within an organoid infection model.

Pharmacological modulation of host factors reduces TBEV replication

Our investigation into the key pathways disrupted by TBEV infection has provided valuable insights for targeted therapy. We selected 17 kinase inhibitors targeting the most differentially regulated kinases, 3 acetylase inhibitors, 6 antagonists of SIRT1 and histone deacetylases, 7 modulators of DNA damage response and 4 autophagy inhibitors (Figs. 6 and S14–16; Supplementary Data 9). The antiviral effects of various drugs and compounds were assessed in both Vero and A549 cells. We chose Vero cells for antiviral examination due to they are routinely used for TBEV isolation, A549 cells were chosen because their susceptibility for TBEV infection[63,64]. Among the 37 drugs tested, an activator of histone deacetylase (ITSA-1) and an autophagy inhibitor (Wortmannin) significantly increased virus growth in both Vero and A549 cells (Figures S15m, w and S16m, w).

We identified pharmacological inhibitors of GSK3, CDKs and CK2 that exhibited a significant impact on TBEV replication. CHIR-98014, an inhibitor of GSK3, displayed an IC_{50} of 0.000045 μM in Vero cells and 0.37 μM in A549 cells, effectively inhibiting TBEV infection. AR-A014418, another inhibitor, demonstrated remarkable antiviral activity by inhibiting more than 50% of the viruses even at a concentration of 10 nM, and achieving approximately 90% inhibition at concentrations of 1,10 and 100 μM in Vero cells, with an IC_{50} of 1.01 μM in A549 cells (Figs. 6a and S14a). In line with observations related to SARS-CoV-2, Dinaciclib, a CDK inhibitor, displayed notable antiviral activity against TBEV, with over 70% inhibition of the virus at a concentration of 10 nM. Meanwhile, CDK2-IN-73 exhibited an inhibitory IC_{50} at 0.00070 μM in Vero cells and 0.0016 μM in A549 cells, respectively (Figs. 6b and S14b). The inhibitor (E/Z)-GO289, targeting CK2, demonstrated a significant antiviral effect in Vero cells, with an IC_{50} of 0.00011 μM, albeit less pronounced antiviral activity in A549 cells, where the IC_{50} was 1.33 μM (Figs. 6c and S14c). Notably, inhibitors of CLK and MAPK showed no significant impact on TBEV replication (Figures S15a–i and S16a–i).

Since TBEV infection induces the acetylation of host proteins, we also investigated the antiviral effects of acetylase inhibitors and deacetylase agonists. CPTH2, an inhibitor of histone acetyltransferase, exhibited significant inhibition of TBEV in both Vero and A549 cells, with the IC_{50} of 0.81 μM and 0.013 μM, respectively (Fig. 6d and S14d). Furthermore, TBEV infection triggers DNA damage response, including the activation of ATM, ATR and DNA-PK. Inhibitors of ATM (AZD-1390) and ATR (VE-822) were found to possess the ability to suppress TBEV replication, while AZD7648, an inhibitor of DNA-PK, exhibited more than 50% suppression of TBEV at all concentrations in Vero cells (Figs. 6e and S14e). TBEV NS5 has been shown to bind to SIRT1, inhibiting DNA damage repair (Fig. 3o). Consistently, we found that activate SIRT1 with resveratrol, nicotinamide riboside chloride (NAM), and SRT1720 significantly inhibited TBEV replication, underscoring the antiviral potential of SIRT1 during TBEV infection (Figs. 6f, S14f, S15t–u and S16t–u). However, inhibiting SIRT1 with selisistat had no discernible effect on TBEV replication, consistent with the findings in SIRT1 KD cells (Figures S15v and S16v). Enoxacin, a molecule that could boost DNA repair, could also inhibit the replication of TBEV at the IC_{50} of 0.00011 μM in Vero cells (Figs. 6f and S14f).

Moreover, we explored the role of autophagy by employing specific inhibitors. The results indicated that Spautin-1 and 3-MA, both autophagy inhibitors, significantly suppressed TBEV replication, exhibiting IC_{50} values of 0.0000027 μM and 0.011 μM, respectively, in Vero cells (Fig. 6g). However, their inhibitory effects on TBEV replication were less pronounced in A549 cells (Figure S14g). Chloroquine, a well-known inhibitor of autophagic flux frequently used to suppress viral replication, also displayed substantial inhibition of TBEV replication, with IC_{50} values of 0.00012 μM in Vero cells and 0.00049 μM in A549 cells (Figs. 6g and S14g). Additionally, we confirmed the effects of pharmacological agents targeting DDR and autophagy on TBEV replication in T98G cells. Consistent with the findings in Vero and A549 cells, treatment with the ATM inhibitor AZD-1390, the SIRT1 agonist Fisetin, and the autophagic flux inhibitor chloroquine significantly reduced TBEV transcription (Figure S17a–c).

Discussion

In this study, we delineate cellular alterations in the proteome, phosphoproteome and acetylproteome following TBEV infection, and uncovered a significant impact of TBEV infection on the innate immune response, ribosomal biogenesis, DNA damage response, and autophagy.

We observed an upregulation in the expression of RIG-I and TLR3, consistent with findings in TBEV-infected neural cells[65,66]. In the cases of DENV and ZIKV, TLR3 activation has been established to stimulate interferon production[67,68]. while TBEV can enhance RIG-I expression to activate interferon secretion[69]. The increased levels of RIG-I and TLR3 likely account for the heightened expression of IFIT1, IFIT2 and OASL during TBEV infection. Importantly, earlier studies have identified functional TLR3 polymorphisms as a risk factor for severe TBEV infection[70,71], and ZIKV-induced TLR3 activation is implicated in virus-induced disruption of neurogenesis[72]. These findings underscore the diverse pathogenic roles of elevated TLR3 during TBEV infection.

Virus-induced interference with the host ribosome biogenesis has been documented for several viruses[73,74]. HSV-1 infection, for instance, reduces the incorporation of 18S and 28S into cytoplasmic ribosomes, thereby limiting the rate of ribosomal biogenesis. Similarly, the HIV Tat protein can disrupt ribosome biogenesis by interacting with the fibrillarin-U3snoRNA complex. In our current study, we demonstrate

https://doi.org/10.1038/s41467-024-54628-w

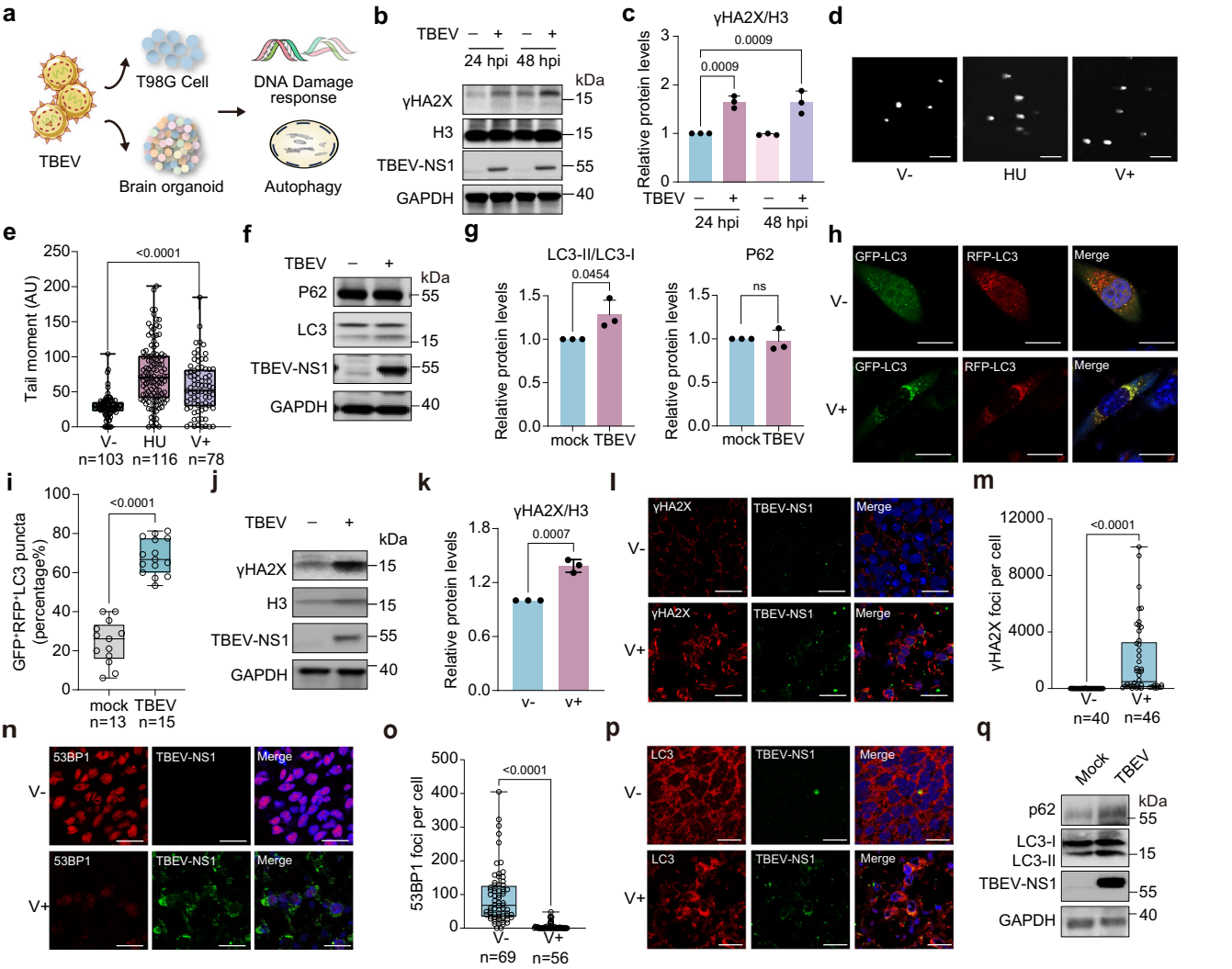

Fig. 5 | TBEV infection regulates the DNA damage response and autophagy in neuronal cells and brain organoids. a DNA damage response and autophagy were determined in TBEV-infected T98G cells and brain organoids. **b** Immunoblot assay showing increased expression of γH2AX in TBEV-infected T98G cells. **c** Quantification of increased percentage of γH2AX /H3 in (**b**). **d** Images of comet assays from mock or TBEV-infected cells. Scale bar, 20 μm. **e** Quantification of comet tail moment shown in (**d**). **f** Immunoblot assay showing increased expression of LC3-II in TBEV-infected cells. **g** Quantification of increased percentage of LC3-II/LC3-I and unchanged p62/GAPDH in (**f**). **h** TBEV-infected cells exhibited a higher number of GFP⁺LC3 puncta compared with mock-infected cells. Scale bar, 20 μm. **i** Quantification of the number of GFP⁺ LC3 puncta per cell confirmed the increase in autophagosomes in TBEV-infected cells. **j** Immunoblot assay showing increased expression of γH2AX in TBEV-infected brain organoids. **k** Quantification of increased percentage of γH2AX /H3 in (**j**). **l** More punctate structures of γH2AX in brain organoids infected with TBEV compared with the control. TBEV NS1 protein used to label infected cells. Nuclei stained with DAPI. Scale bar, 100 μm. **m** Quantification of indicated puncta in (**l**), each dot is a nucleus. **n** Less punctate structures of 53BP1 in brain organoids infected with TBEV compared with the control. TBEV NS1 protein used to label infected cells. Nuclei were stained with DAPI. Scale bar, 100 μm. **o** Quantification of indicated puncta in (**n**), each dot is a nucleus. **p** The brain organoid infected with TBEV exhibited an increase number of GFP⁺LC3 puncta compared to mock-infected organoid. Scale bar, 100 μm. **q** Immunoblot assay of TBEV-infected brain organoids revealed increased expression levels of LC3 and P62. Each point represents a sample. Data are represented as mean ± SEM of 3 independent experiments. The *P*-values are calculated and reported using one-way ANOVA (**c**, **g**, **k**). For all boxplots (**e**, **m**, **o**), median, upper and lower quartile as well as significance levels of *P* values from two-sided Wilcoxon test are shown. Source data are provided as a Source Data file.

that TBEV infection also results in a reduction in the transcripts of 18S and 28S rRNAs, mediated by TBEV NS5. The impaired ribosomal biogenesis can induce translational shut-off, aligning with the significantly decreased abundance of host proteins observed in our study and corroborated by previous research[48].

While the interplay between some DNA viruses and DNA damage response (DDR) has been extensively studied, present understanding of such interactions with RNA viruses, including TBEV, remains comparatively limited[52]. We demonstrate that TBEV infection induces DNA damage by activating ATM, ATR and DNA-PK, along with the formation of γH2AX foci. In contrast, ZIKV infection activates ATM, but suppresses ATR in the activation of DNA damage response[75,76]. For HCV, NS3-NS4A and NS5B interact with ATM, which is essential for HCV RNA replication, while DENV infection does not significantly impact DDR. These studies highlight distinct regulatory mechanisms of DDR among different flaviviruses. In addition to inducing DNA damage, TBEV inhibits its repair through the interaction of NS5 with SIRT1. SIRT1 is known to promote DNA repair activity by deacetylating KAP1 and Ku70[56,57]. We observed that both NS5 overexpression and TBEV infection led to elevated acetylation of KAP1 and Ku70, consequently inhibiting DNA repair activity. SIRT1 has been implicated in various roles during viral infection. For instance, the HBx protein of Hepatitis B virus binds to SIRT1 to enhance viral transcription[77], while the HIV Tat protein interacts with SIRT1 to block the deacetylate of NF-κB, promoting the hyperactivation of CD4 + T cells[78,79]. Our results reveal a function of SIRT1 engaged by TBEV infection, suggesting the pathogenic role of

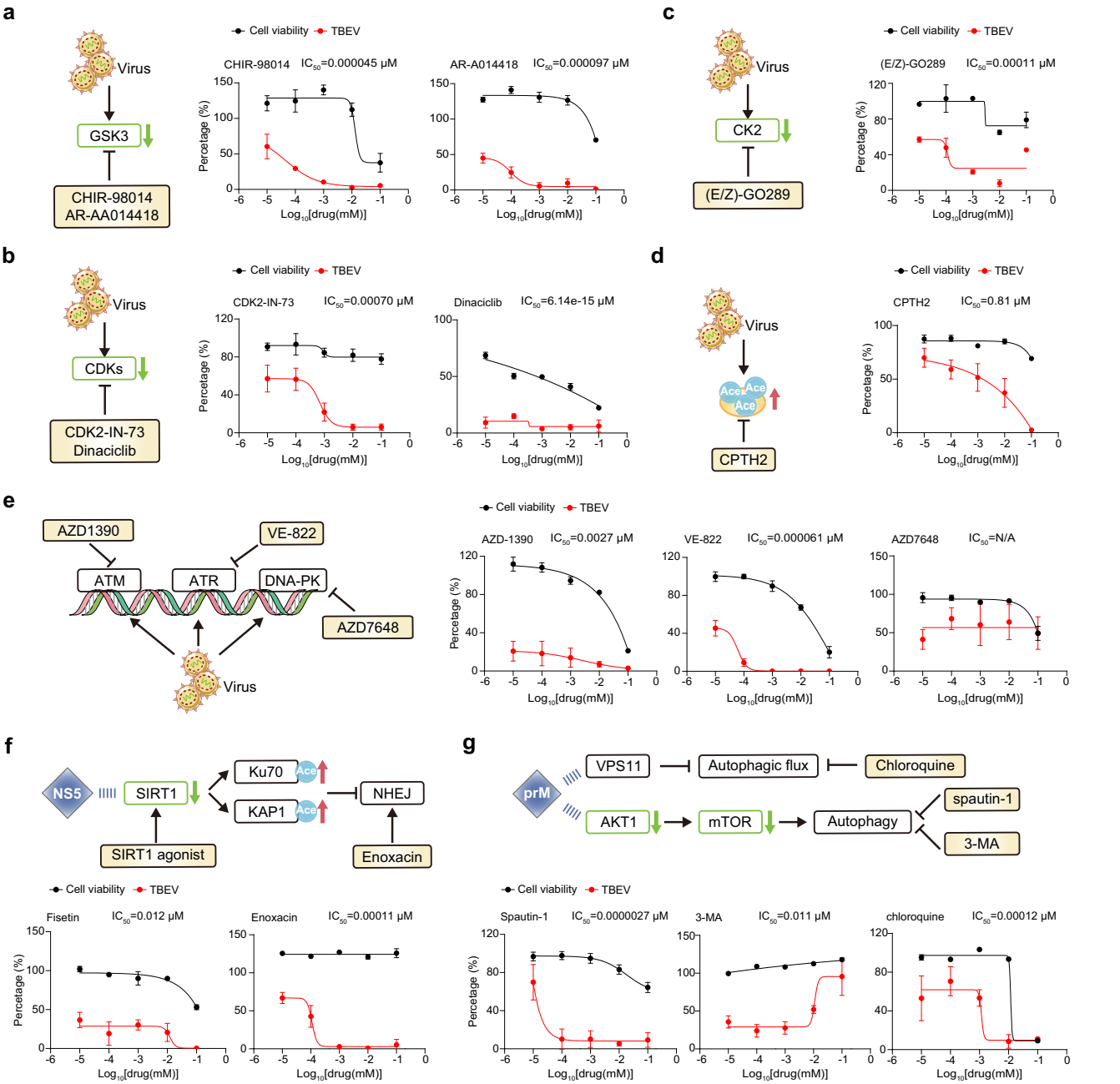

Fig. 6 | Pharmacological modulation of host factors reduces TBEV replication. **a** TBEV infection was predicted to inhibit the activity of GSK3. Vero cells were pre-treated with inhibitors of GSK3, CHIR-98014 and AR-A014418, followed by TBEV infection for 48 h. IC_{50} was determined by probe PCR. The cell viability was measured by cell counting (CCK-8) assay without viral infection. Percent of viral titer compared with DMSO treatment (red) and cell viability (black) depicted. Error bars represent the mean ± SEM of three biological replicates. **b**, **c** Similar to (**a**), Vero cells were treated with the CDK2 inhibitor CDK2-IN-73, Dinaciclib (**b**) and CK2 inhibitor, (E/Z)-GO289 (**c**). **d** TBEV infection elevates host protein acetylation. A549 cells were pre-treated with the inhibitor of acetylase (CPTH2) before TBEV infection. **e** TBEV infection activates ATM, ATR and DNA-PK to trigger DNA damage response. Vero cells were pre-treated with the inhibitors of ATM (AZD-1390), ATR (VE-822) and DNA-PK (AZD7648) before TBEV infection. **f** TBEV NS5 binds SIRT1 to suppress DNA damage repair. Vero cells were pre-treated with the agonist of SIRT1 (Fisetin) and damage repairment (Enoacxin) before TBEV infection. **g** TBEV prM interacts with AKT1 and VPS11 to regulate autophagy. Vero and A549 cells were pre-treated with autophagy inhibitors (Spautin-1 and 3-MA) and autophagic flux inhibitor (chloroquine) before TBEV infection. Data are represented as mean ± SEM of 3 independent experiments. Source data are provided as a Source Data file.

SIRT1 during TBEV infection, which could be used as a promising antiviral target for TBEV infection.

The impact of TBEV infection on autophagy remains controversial, with some studies suggesting activation of autophagy and others claiming no induction during TBEV infection[80,81]. Our findings, including induced LC3 transition, the formation of LC3 puncta, and autophagosomes upon TBEV infection, provide robust evidence supporting in induction of autophagy by TBEV. We further demonstrate that prM interacts with AKT1 and inhibits AKT1-mTOR signaling, leading to autophagy induction. The activation of autophagy via suppressing AKT1-mTOR is a shared feature with ZIKV and SARS-CoV-2 infections[59,60]. Although TBEV infection initially activates AKT1 at 2 h, a subsequent reduction is observed at 24 and 48 h after virus infection. This phenomenon is akin to observations in HCV-infected cells, where transiently activated AKT1 was suggested to promote HCV entry[82]. Similarly, activated AKT1 has been shown to promote the entry of

Ebola virus[83]. It is plausible that TBEV activates AKT1 during the early infection phase to facilitate host cell entry and subsequently suppresses AKT1 to induce autophagy, promoting virus replication during the late infection phase. In addition to inducing autophagy, TBEV also manipulates autophagic flux by interacting with the HOPS complex, specifically VPS11. Viral proteins frequently hijack the HOPS components to enhance viral replication. For instance, SARS-CoV-2 ORF3a interacts with VPS39 to inhibit autophagic flux[61], and the African swine fever virus CP204L interacts with VPS39 to facilitate ASFV replication and assembly[62]. Further investigation is warranted to elucidate how the interaction of prM with AKT1 and VPS11 contributes to promoting viral replication.

We tested the antiviral activity of 37 drugs and compounds, including several FDA approved, or clinically-trialed substances such as LY2090314 (GSK3, FDA approved), dinaciclib (CDK, FDA approved), silmitasertib (CK2, FDA approved), resveratrol (SIRT1, FDA approved), fisetin and NAM (SIRTs agonists, FDA approved), VE-822 (ATR, phase I), AZD7648 (DNA-PK, phase II), AZD1390 (ATM, phase I), enoxacin (DNA repair booster, FDA approved), and chloroquine (autophagy, FDA approved). Notable, dinaciclib, an inhibitor of CDKs, showed inhibitory effects on SARS-CoV-2 and DENV[84,85]. GSK3, previously implicated as a promoting factor for various viruses, was targeted by CHIR-98014[86], resulting in inhibiting HCV replication and HIV-mediated neurotoxicity[87,88]. VE-822, an ATR inhibitor, exhibited potent antiviral activity against SARS-CoV-2 and HSV-1[89,90]. Enoxacin, an FDA-approved antibacterial agent, demonstrated the ability to boost DNA repair and reduce the replication of SARS-CoV-2 and ZIKV[91–93]. SIRT1, identified as a key player in TBEV infection, showed significant inhibition of viral replication upon overexpression. This effect was mirrored by the addition of SIRT1 agonists, including FDA-approved fisetin and NAM, along with universally used agonists like SRT2183 and SRT1720, highlighting SIRT1 as a promising antiviral target for TBEV. Chloroquine, a non-specific antiviral agent, demonstrated efficacy against TBEV in both Vero and A549 cells, echoing its inhibitory effects on DENV and its protective role against ZIKV-induced mortality and microcephaly[94,95]. However, further investigation is warranted to ascertain whether chloroquine also functions in protecting against TBEV-induced neuropathology. Moreover, we noticed that certain drugs showed greater effectiveness in Vero cells, which might be partially attributed to the distinct interferon responses characteristic of various cell lines (Figure S17d–e). However, the diverse origins of cell lines are associated with variations in cellular signaling, metabolic processes, and interferon responses, which may result in differing sensitivities to viral infections and responses to drug treatments. In this context, we have decided to evaluate the efficacy of the antiviral drugs in various cells, such as Vero, A549, and T98G cells, as this approach is likely to generate more comprehensive data for future in vivo evaluations of antiviral therapies.

In summary, our comprehensive proteomics approaches shed light on the cellular processes manipulated during TBEV infection, providing insights into the underlying pathogenic mechanisms. Addressing the imperative for enhanced therapeutic strategies against TBEV, we conducted a data-guided drug screen, showcasing the efficacy of our integrated analysis across various levels. We anticipate that further exploration of this extensive dataset from our study, through additional studies delving into the interplay between different omics levels, will significantly advance our understanding of the pathogenesis and offer insights for developing effective antiviral drugs against TBEV and other tick-borne flaviviruses.

Methods

Ethics statement

All infectious experiments involving mice were conducted in the BSL-3 facility at the Changchun Veterinary Research Institute, Chinese Academy of Agricultural Sciences. The protocol was reviewed and approved by the Animal Welfare and Ethics Committee of Jilin University (2023-0166). The generation of brain organoids and the related experiments was approved by the Medical Ethics Committee of the First Affiliated Hospital of Jilin University (2023-661). Informed consent was obtained from participants who provided peripheral blood samples for the purpose of inducing pluripotent stem cells.

Cell lines and reagents

HEK293T, A549, T98G, and Vero cells were cultured in Dulbecco's Modified Eagle Medium (DMEM, HyClone, Logan, USA) supplemented with 10% fetal bovine serum (BBI, Shanghai, China) and 1% penicillin-streptomycin (100 IU/ml) at 37°C with 5% CO_2. All cells were verified to be mycoplasma-free.

Virus strain and in vitro infection

The TBEV strain, classified as the Far Eastern subtype, was isolated from *Ixodes persulcatus* ticks in northeastern China[96]. The virus was propagated in Vero cells and titrated via tissue culture median infectious dose assay ($TCID_{50}$). All experiments involving TBEV infection were conducted in a Biosafety Level 3 (BSL-3) laboratory.

Vero cells were infected with TBEV at a MOI (multiplicity of infection) of 2.0 for the subsequent experiments. Cells in mock infection group were treated with an equal volume of culture medium. Cell samples were collected and washed with PBS at 2, 6, 12, 24, and 48 h post-infection (hpi). Subsequently, cells were lysed in sodium deoxycholate (SDS) lysis buffer (100 mM Tris-HCl pH 8.5; 4% SDS) supplemented with protease inhibitor cocktail III and inhibitors of deacetylation including nicotinamide (NAM) and trichostatin A (TSA). The collected samples were then subjected to proteome, phosphoproteome, and acetylproteome analysis.

Plasmids and siRNA

The TBEV structural and nonstructural proteins (GenBank Access Number MN615726.1) were cloned into Flag-VR1012, incorporating 2×Strep II affinity and 3×Flag tags at the N terminus (Sangon Biotech, Shanghai, China). Additional plasmids, such as HA-SIRT1, HA-SIRT1-H363Y, Myc-Ku70, Myc-AKT1, GFP-LC3, GFP-RFP-LC3, and Myc-VPS11, were purchased from Miaoling Biotech (Wuhan, China).

For small interfering RNA (siRNA) targeting ATG7, oligonucleotide with the sequences of siRNA-1 (5′-GGGUUAUUACUACAAUGGUG-3′) and siRNA-2 (5′-GGAGUCACAGCUCUUCCUU-3′) were synthesized at Sangon Biotech(Shanghai, China)[60,97].

Proteome, phosphoproteome and acetylproteome analysis

The mock and TBEV-infected Vero cell samples collected at 2, 6, 12, 24, and 48 hpi underwent lysis by sonication, followed by centrifugation at 12,000 g for 15 min at 4 °C to remove cell debris. The resulting supernatants were transferred to a new centrifuge tube, and the protein concentration was determined using a BCA kit (Thermo, Waltham, USA). Equal amounts of protein from each sample were acetone-precipitated and subjected to trypsin digestion for mass spectrometry analysis to determine total protein abundance, phosphorylation, and acetylation.

Liquid chromatography-mass spectrometry (LC-MS) based proteomics was conducted by PTM BioLab Co., Ltd., Hangzhou, China. Briefly, the peptides were separated using the NanoElute system (Bruker) and separated by an ultra-high-performance liquid phase system. The system was injected into a Capillary ion source for ionization and subsequently analyzed by timsTOF Pro mass spectrometer (Bruker). The peptide precursor ions and their secondary fragments were detected and analyzed using high-resolution TOF using Parallel Accumulation Serial Fragmentation (PASEF) mode.

Bioinformatics analysis

The acquired tandem mass spectrometry data were processed using the MaxQuant software (version 1.6.17.0). The employed protein

databases encompassed the *Chlorocebus sabaeus* proteome (Blast_Chlorocebus_sabaeus_60711_PR_20210928), the mycoplasma proteome (uniprot-reviewed_yes+AND+organism_mycoplasma), and relevant TBEV proteins (GenBank: QLL99542.1). To obtain human protein data, we mapped *Chlorocebus sabaeus* proteins to their human orthologs using the biomaRt R package (https://bioconductor.org/packages/release/bioc/html/biomaRt.html). For proteolytic digestion, Trypsin/P was the enzyme of choice. For the proteomics dataset, cysteine carbamidomethylation (Carbamidomethyl (C)) was set as a fixed modification, with methionine oxidation and protein N-terminal acetylation considered as variable modifications. In addition to these modifications, lysine acetylation, as well as phosphorylation of serine, threonine, and tyrosine, were included as additional variable modifications in the phosphoproteomics and acetylomics analyses. To ensure the reliability of our findings, both protein identification and peptide-spectrum match (PSM) validation were rigorously maintained at a 1% false discovery rate (FDR).

For the analysis of different peptides at 2, 6, 12, 24, and 48 hpi, we normalized peptide intensities across different samples using centralization transformation, followed by statistical analysis with Student's t-test.

Sequence alignment analysis of homologous proteins

Protein sequences for TBEV (MN615726.1), and additional flaviviruses (LIV: NC_001809.1, OHFV: NC_005062.1, LGTV: NC_003690.1, POWV: NC_003687.1, YFV: NC_002031.1, ZIKV: NC_012532.1, JEV: NC_001437.1, DENV: NC_001474, WNV: NC_001563.2) were retrieved from the GenBank database at the National Center for Biotechnology Information (NCBI). Multiple sequence alignment was conducted using the CLUSTALW tool available at https://www.genome.jp/tools-bin/clustalw.

Mapping of phosphorylated and acetylated sites on the NS3 and NS5 structures

The homology modeling module for NS3 and NS5 was conducted in Discovery Studio (2019)[98]. Template structures for NS3 and NS5 were obtained from the Protein Data Bank. Phosphorylation and acetylation sites were visually inspected and mapped using the PyMOL software (https://pymol.org). Phosphorylation on NS3 and NS5 were simulated in silico by using the PyTMs plugin as implemented in PyMOL[99]. Poisson-Boltzmann electrostatic surface potential of native and post-translationally modified NS3 and NS5 were calculated using the PBEQ Solver tool on the CHARMM-GUI server by preserving existing hydrogen bonds[100]. Molecular graphics depictions were produced with the PyMOL software.

Gene enrichment and kinase activity analysis

To conduct gene enrichment analysis, we utilized the Gene Ontology (GO) database (version 3.14.0), Kyoto Encyclopedia of Genes and Genomes (KEGG) database (version 3.14.0), String database (version 12.0), and DAVID database (version December, 2021). The Kinase-Substrate (K-S) Enrichment Analysis (KSEA) was performed using the R package KSEA app[29,101–103].

Co-immunoprecipitation and immunoblotting assay

For the co-immunoprecipitation assay, cells lysed with IP buffer were centrifuged at 15,000 g, 4 °C for 15 min to remove debris. The supernatants were then incubated overnight with ANTI-FLAG® M2 Affinity Gel (Sigma-Aldrich, St. Louis, USA), ANTI-HA or ANTI-MYC Affinity Gel (Millipore, Billerica, USA). Following incubation, these lysates were washed five times with 1 ml IP buffer and boiled at 100 °C for 10 min. Cell lysates and bound proteins were separated by SDS-PAGE, and then transferred onto PVDF membrane. The proteins were subsequently detected using the primary antibodies against Flag tag (proteintech, 66008-4-Ig), MYC tag (proteintech, 60003-2-Ig), TBEV NS1 (R&D Systems, MAB10106), HA tag (proteintech, 51064-2-AP), phosphor-KAP1 (Ser824) (abcam, ab133440), gamma H2A.X (Ser139) (abcam, ab81299), 53BP1 (abcam, ab175933), pan acetylation (proteintech, 66289-1-Ig), Vinculin (proteintech, 66305-1-Ig), Ku70 (Zen-Bioscience, 200995), Ku80 (Zen-Bioscience, 201004), LC3 (proteintech, 14600-1-AP), phospho-ATM (Ser1981) (Zen-Bioscience, 380751), ATM (Zen-Bioscience, R23317), phosphor-ATR (T1989) (abcam, ab223258), ATR (Zen-Bioscience, 161471), KAP1 (Zen-Bioscience, R24790), phospho-AKT1 (Ser473) (Zen-Bioscience, 381555), phospho-AKT1 (Thr308) (Zen-Bioscience, 341790), AKT1 (proteintech, 80457-1-RR), phospho-mTOR (Ser2448) (Zen-Bioscience, 381557), mTOR (Zen-Bioscience, 380411), VPS11 (Zen-Bioscience, R389076), VPS41 (Zen-Bioscience, R26098), LAMP1 (Beyotime, AF7353) and VPS11 (Zen-Bioscience, R389082) were used for immunoblotting analysis. The membranes were then incubated with indicated secondary antibodies and the bands were determined with ChemiDoc XRS + Molecular Imager software (Bio-Rad, Philadelphia, USA).

Immunofluorescence analysis

Immunofluorescence assays were carried out in cultured cells. Specifically, cells were fixed with 4% paraformaldehyde for 30 min and then permeabilized with 1% triton in 1×PBS for 10 min at room temperature. The cells were then blocked with 2% BSA for 1 h at room temperature and stained with the primary antibodies listed above and secondary antibodies including CoraLite488-conjugated Goat Anti-Rabbit IgG(H + L) (proteintech, SA00013-2), CoraLite594-conjugated Goat Anti-Mouse IgG(H + L) (proteintech, CL594-67243) and CoraLite 647-Goat Anti-Mouse Recombinant Secondary Antibody (H + L) (proteintech, RGAM005). The nuclei were labeled with DAPI. Data analyses were carried out using ImageJ 1.52.

Comet assay

The comet assay, following the protocol of Collins with minor modifications[104]. Cell suspensions were mixed with 0.7% low-melting-point agarose for gel preparation. After solidification, the embedded cells were lysed at 4 °C overnight. Slides were then placed in an alkaline electrophoresis solution for 20 min at 4 °C for unwinding, followed by electrophoresis in the same solution for 20 min at a voltage gradient of 0.8 V/cm across the platform in a horizontal electrophoresis chamber. Subsequently, the slides were rinsed once with cold PBS, washed twice in cold distilled water, and left to dry. After drying, slides were stained with 1 μM Propidium Iodide for 30 min in the dark and then rinsed twice in distilled water. After DNA staining, analysis was performed using fluorescence microscopy (Olympus Biosystems). The tail moment was measured using the OpenComet plugin for Fiji software.

NHEJ repair assay

Stable expression of EJ5-GFP was established in HEK293T cells. In brief, pimEJ5-GFP expression plasmids were transfected into HEK293T cell. The cells stably expressed pimEJ5-GFP underwent selection and maintenance within a medium containing 2 μg/ml puromycin. To observe the localization of double-strand break (DSB), EJ5-GFP cells were transfected with a pCBASceI expressing plasmid and subsequently infected with TBEV, or transfected with TBEV NS5. Cells were grown for 48 h and processed for further flow cytometry analysis.

Probe PCR and qPCR

Virus RNA in the supernatants were extracted by the TIANamp Virus RNA kit (Tiangen, Beijing, China), and cDNA was synthesized using PrimeScript 1st Strand cDNA Synthesis kit (TaKaRa). Copies of the TBEV virus was detected using probe PCR using the forward primer: 5′-GGGCGGTTCTTGTTCTCC-3′, reverse primer: 5′-ACACATCACCTCCTTGTCAGACT-3′ and the probe: FAM-TGAGCCACCATCACCCAGACACA-BHQ1.

For the detection of cellular inflammatory factors. Cellular RNA was extracted from mock and TBEV-infected cells, followed by reverse

transcription into cDNA. qPCR was then employed to assess the expression level of IL1A, NFKB, IL6, IL8 and CXCL10 using primers listed in Supplementary Data 10.

Cell cycle analysis by flow cytometry

Mock-infected cells or cells infected with TBEV at the MOI of 0.1, 1.0 and 10 were collected at 48 hpi and fixed in 70% ethanol overnight at 4 °C. The cells were then washed with PBS once and stained with PI/RNase Staining Buffer Solution (BD Biosciences, California, USA) for 15 min in the dark. The cell cycle distribution was analyzed using a BD LSRFortessa flow cytometer. Data analysis was carried out using ModFit LT 5.0 (Verity Software House, Maine, USA).

Senescence-associated β-galactosidase staining

Senescence-associated β-galactosidase staining was performed using a senescence-β galactosidase staining kit (Beyotime, C0602) following the manufacturer's instructions. Briefly, the cells were initially washed once with PBS, after which 1 mL of β-galactosidase staining fixative was added, and the cells were fixed at room temperature for 15 min. The fixative was then aspirated, and the cells were washed three times with PBS, with each wash lasting 3 min. Following centrifugation and removal of PBS, 0.5 mL of the staining working solution was added to each tube, and the cells were incubated overnight at 37 °C. Finally, the stained cells were examined under a standard optical microscope.

Cell apoptotic assessment

To assess apoptotic cells, we utilized the Annexin-V/Caspase-3 kit (Beyotime, C1077S) following the manufacturer's instructions. Cells cultured in 24-well plates were centrifuged at 1000 × *g* for 5 min. After aspirating the cell culture medium, the cells were washed once with PBS. Subsequently, a mixture of 194 μL Annexin V-mCherry Binding Buffer, 5 μL Annexin V-mCherry and 1 μL GreenNuc™ Caspase-3 Substrate were gently prepared and added to the cells. The cells were then incubated at room temperature in the dark for 30 min. Finally, the cells were observed under a fluorescence microscope, where GreenNuc™-DNA emitting green fluorescence (Ex/Em=500/530 nm) and Annexin V-mCherry emitting red fluorescence (Ex/Em=587/610 nm).

Mice infected with TBEV

Six-week-old female BALB/c mice purchased from Changsheng Biotechnology (Benxi, China) were used for TBEV infection. The mice were maintained at 22 °C, 70% humidity, and subjected to a 12-h light-dark cycle. Five mice served as control were mock-infected, while another group of five mice were inoculated intraperitoneally with 10^3 pfu of TBEV and monitored daily for clinical symptoms following inoculation. At designated time points, the mice were anesthetized and perfused with 4% paraformaldehyde (PFA) to fix the tissues. Brain tissues were subsequently collected and stored in 4% PFA for further experiments.

Brdu staining

Cells were pulse-labeled with 100 μM BrdU (Beyotime) at 37 °C in the dark for 1 h. Following incubation, the cells were rinsed with PBS and fixed in 75% ethanol at 4 °C overnight. The samples were then treated with 2 N HCl–0.5% Triton X-100 in the dark for 30 min and subsequently neutralized with 0.1 M sodium tetraborate. The samples were stained with anti-BrdU antibody (proteintech, China) in PBS containing 0.5% Tween 20 and 1% BSA, followed by incubation with indicated AF488 conjugated second antibody. The stained cells were then resuspended in PI staining solution (BD bioscience, USA) and analyzed by flow cytometry.

Analysis of protein-protein interaction and the structure of viral proteins using AlphaFold3

The interaction between NS5 (PDB:7D6N) and SIRT1 (PDB:4IG9), prM (GenBank: QLL99542.1) and AKT1 (uniprot: P31749), prM and VPS11 (uniprot: Q9H270), NS2B3 (GenBank: QLL99542.1) and STX17 (uniprot: P56962) was analyzed using the AlphaFold3 online platform (https://deepmind.google/technologies/alphafold/), and the results were visualized using PYMOL.

Generation of brain organoids

The brain organoids were generated using brain organoid generation kit from Guidon Pharmaceutics (Beijing, China). Briefly, induced pluripotent stem cells (iPSC) were dissociated into single-cell suspension using accutase. Subsequently, approximately 9000 cells were seeded into PrimeSurface low-adhesion 96-well plates in 100 μL of embryoid body (EB, containing mTeSR 1 (Stem Cell) + 50 μM Y27632 (MCE)). The medium was replaced every two days to support the growth and development of the embryoid bodies. Upon reaching a diameter of 500-600 μM with clear boundaries, the EBs were transferred to a low-adhesion 24-well plate, and 1 ml of neural induction medium was added to initiate the differentiation of primitive neuroepithelial cells. After 4 days of static culture using medium without Vitamin A, the organoids were transferred to a 37 °C shaking incubator, which were cultured with medium containing Vitamin A until use.

Transmission electron microscopy and electron tomography

A549 cells were either mock-infected or infected with TBEV for 3 days. The samples were collected and fixed with a 2.5% glutaraldehyde solution in 0.1 M sodium cacodylate buffer, followed by post-fixation with 1% osmium tetroxide and 1% potassium ferrocyanide. After washing with ddH_2O, the samples were dehydrated using increasing concentrations of ethanol solutions, and embedded in epoxy resin. The ultrathin sections were stained with 2% uranyl acetate and lead citrate, images were then examined with a transmission electron microscope.

Statistical significance

Statistical significance was assessed using the Student's *t*-test to determine *P*-values. Enrichment analyses for GO and KEGG pathways were conducted employing clusterProfiler package within R (version 4.0.4), utilizing default parameters.

Reporting summary

Further information on research design is available in the Nature Portfolio Reporting Summary linked to this article.

Data availability

All original mass spectrometry data of this paper are publicly accessible and have been deposited in the ProteomeXchange partner repository (http://www.proteomexchange.org/) under accession number PXD048439. All other study data are included in the main text and/or supporting information. Source data are provided with this paper.

Code availability

The data of this study were analyzed with standard software that is already available and does not require a custom code.

References

1. Pierson, T. C. & Diamond, M. S. The continued threat of emerging flaviviruses. *Nat. Microbiol* **5**, 796–812 (2020).
2. Deviatkin, A. A., Kholodilov, I. S., Vakulenko, Y. A., Karganova, G. G. & Lukashev, A. N. Tick-borne encephalitis virus: an emerging ancient zoonosis? *Viruses* **12**, 247 (2020).
3. Madison-Antenucci, S., Kramer, L. D., Gebhardt, L. L. & Kauffman, E. Emerging tick-borne diseases. *Clin. Microbiol. Rev.* **33**, e00083–18 (2020).
4. Lindquist, L. & Vapalahti, O. Tick-borne encephalitis. *Lancet* **371**, 1861–1871 (2008).

5. Worku, D. A. Tick-borne encephalitis (TBE): from tick to pathology. *J. Clin. Med.* **12**, 6859 (2023).
6. Dobler, G. et al. Tick-borne encephalitis virus vaccination breakthrough infections in Germany: a retrospective analysis from 2001 to 2018. *Clin. Microbiol. Infect.* **26**, 1090.e1097–1090.e1013 (2020).
7. Dai, X., Shang, G., Lu, S., Yang, J. & Xu, J. A new subtype of eastern tick-borne encephalitis virus discovered in Qinghai-Tibet Plateau, China. *Emerg. Microbes Infect.* **7**, 74 (2018).
8. Sukhorukov, G. A. et al. The Baikal subtype of tick-borne encephalitis virus is evident of recombination between Siberian and Far-Eastern subtypes. *PLoS Negl. Trop. Dis.* **17**, e0011141 (2023).
9. Im, J. H. et al. Geographic distribution of tick-borne encephalitis virus complex. *J. Vector Borne Dis.* **57**, 14–22 (2020).
10. Kemenesi, G. & Bányai, K. Tick-borne flaviviruses, with a focus on Powassan virus. *Clin. Microbiol. Rev.* **32**, e00106–17 (2019).
11. Tang, J. et al. Sterile 20-like kinase 3 promotes tick-borne encephalitis virus assembly by interacting with NS2A and prM and enhancing the NS2A-NS4A association. *J. Med. Virol.* **95**, e28610 (2023).
12. Yang, Q. et al. Tick-borne encephalitis virus NS4A ubiquitination antagonizes type I interferon-stimulated STAT1/2 signalling pathway. *Emerg. Microbes Infect.* **9**, 714–726 (2020).
13. Sui, L. et al. Flavivirus prM interacts with MDA5 and MAVS to inhibit RLR antiviral signaling. *Cell Biosci.* **13**, 9 (2023).
14. Gracias, S. et al. Tick-borne flavivirus NS5 antagonizes interferon signaling by inhibiting the catalytic activity of TYK2. *EMBO rep.* **24,** e57424(2023).
15. Akaberi, D. et al. Targeting the NS2B-NS3 protease of tick-borne encephalitis virus with pan-flaviviral protease inhibitors. *Antivir. Res* **190**, 105074 (2021).
16. Kumar, R., Mehta, D., Mishra, N., Nayak, D. & Sunil, S. Role of host-mediated post-translational modifications (PTMs) in RNA virus pathogenesis. *Int. J. Mol. Sci.* **22**, 323(2020).
17. Dawson, A. R. & Mehle, A. Flu's cues: Exploiting host post-translational modifications to direct the influenza virus replication cycle. *PLoS Pathog.* **14**, e1007205 (2018).
18. Stukalov, A. et al. Multilevel proteomics reveals host perturbations by SARS-CoV-2 and SARS-CoV. *Nature* https://doi.org/10.1038/s41586-021-03493-4 (2021).
19. Pinto, S. M. et al. Multi-OMICs landscape of SARS-CoV-2-induced host responses in human lung epithelial cells. *iScience* **26**, 105895 (2023).
20. Ganaie, S. S. et al. Lrp1 is a host entry factor for Rift Valley fever virus. *Cell* **184**, 5163–5178.e5124 (2021).
21. Devignot, S. et al. Low-density lipoprotein receptor-related protein 1 (LRP1) as an auxiliary host factor for RNA viruses. *Life Sci Alliance* **6**, e202302005 (2023).
22. Beatman, E. L. et al. Alpha-synuclein expression restricts RNA viral infections in the brain. *J. Virol.* **90**, 2767–2782 (2015).
23. Santerre, M. et al. HIV-1 Vpr protein impairs lysosome clearance causing SNCA/alpha-synuclein accumulation in neurons. *Autophagy* **17**, 1768–1782 (2021).
24. Link, N. et al. Mutations in ANKLE2, a ZIKA virus target, disrupt an asymmetric cell division pathway in drosophila neuroblasts to cause microcephaly. *Dev. Cell* **51**, 713–729.e716 (2019).
25. Ruzek, D. et al. Morphological changes in human neural cells following tick-borne encephalitis virus infection. *J. Gen. Virol.* **90**, 1649–1658 (2009).
26. Haas, K. M. et al. Proteomic and genetic analyses of influenza A viruses identify pan-viral host targets. *Nat. Commun.* **14**, 6030 (2023).
27. Badia, R. et al. SAMHD1 is active in cycling cells permissive to HIV-1 infection. *Antivir. Res* **142**, 123–135 (2017).
28. Kim, E. T. et al. SAMHD1 modulates early steps during human cytomegalovirus infection by limiting NF-kappaB activation. *Cell Rep.* **28**, 434–448.e436 (2019).
29. Wiredja, D. D., Koyutürk, M. & Chance, M. R. The KSEA App: a web-based tool for kinase activity inference from quantitative phosphoproteomics. *Bioinformatics* **33**, 3489–3491 (2017).
30. Scaturro, P. et al. An orthogonal proteomic survey uncovers novel Zika virus host factors. *Nature* **561**, 253–257 (2018).
31. Carletti, T. et al. Viral priming of cell intrinsic innate antiviral signaling by the unfolded protein response. *Nat. Commun.* **10**, 3889 (2019).
32. Klemm, S. L., Shipony, Z. & Greenleaf, W. J. Chromatin accessibility and the regulatory epigenome. *Nat. Rev. Genet* **20**, 207–220 (2019).
33. Ortega, E. et al. Transcription factor dimerization activates the p300 acetyltransferase. *Nature* **562**, 538–544 (2018).
34. Thompson, P. R. et al. Regulation of the p300 HAT domain via a novel activation loop. *Nat. Struct. Mol. Biol.* **11**, 308–315 (2004).
35. Kerr, S. A. et al. Computational and functional analysis of the virus-receptor interface reveals host range trade-offs in new world arenaviruses. *J. Virol.* **89**, 11643–11653 (2015).
36. Ma, H. et al. M phase phosphorylation of the epigenetic regulator UHRF1 regulates its physical association with the deubiquitylase USP7 and stability. *Proc. Natl Acad. Sci. USA* **109**, 4828–4833 (2012).
37. Wang, M. et al. UHRF1 deficiency inhibits alphaherpesvirus through inducing RIG-I-IRF3-mediated interferon production. *J. Virol.* **97**, e0013423 (2023).
38. Giese, S. et al. Role of influenza A virus NP acetylation on viral growth and replication. *Nat. Commun.* **8**, 1259 (2017).
39. Giraldo, M. I. et al. Envelope protein ubiquitination drives entry and pathogenesis of Zika virus. *Nature* **585**, 414–419 (2020).
40. Sabariegos, R. et al. Akt Phosphorylation of Hepatitis C Virus NS5B Regulates Polymerase Activity and Hepatitis C Virus Infection. *Front Microbiol* **12**, 754664 (2021).
41. Yang, J. et al. Crystal structure of a tick-borne flavivirus RNA-dependent RNA polymerase suggests a host adaptation hotspot in RNA viruses. *Nucleic acids Res.* **49**, 1567–1580 (2021).
42. Lee, E. et al. Structures of flavivirus RNA promoters suggest two binding modes with NS5 polymerase. *Nat. Commun.* **12**, 2530 (2021).
43. Coyaud, E. et al. Global interactomics uncovers extensive organellar targeting by Zika virus. *Mol. Cell. Proteom.* **17**, 2242–2255 (2018).
44. Shah, P. S. et al. Comparative flavivirus-host protein interaction mapping reveals mechanisms of dengue and Zika virus pathogenesis. *Cell* **175**, 1931–1945.e1918 (2018).
45. Choi, Y., Bowman, J. W. & Jung, J. U. Autophagy during viral infection - a double-edged sword. *Nat. Rev. Microbiol* **16**, 341–354 (2018).
46. Poehler, A.-M. et al. Autophagy modulates SNCA/α-synuclein release, thereby generating a hostile microenvironment. *Autophagy* **10**, 2171–2192 (2014).
47. Rutherford, N. J., Moore, B. D., Golde, T. E. & Giasson, B. I. Divergent effects of the H50Q and G51D SNCA mutations on the aggregation of alpha-synuclein. *J. Neurochem.* **131**, 859–867 (2014).
48. Selinger, M. et al. Tick-borne encephalitis virus inhibits rRNA synthesis and host protein production in human cells of neural origin. *PLoS Negl. Trop. Dis.* **13**, e0007745 (2019).
49. Polo, S. E. & Jackson, S. P. Dynamics of DNA damage response proteins at DNA breaks: a focus on protein modifications. *Genes Dev.* **25**, 409–433 (2011).
50. Chmielewska, A. M. et al. The role of IFITM proteins in tick-borne encephalitis virus infection. *J. Virol.* **96**, e0113021 (2022).

51. Di Micco, R., Krizhanovsky, V., Baker, D. & d'Adda di Fagagna, F. Cellular senescence in ageing: from mechanisms to therapeutic opportunities. *Nat. Rev. Mol. Cell Biol.* **22**, 75–95 (2021).
52. Weitzman, M. D. & Fradet-Turcotte, A. Virus DNA Replication and the Host DNA Damage Response. *Annu. Rev. Virol.* **5**, 141–164 (2018).
53. Hustedt, N. & Durocher, D. The control of DNA repair by the cell cycle. *Nat. Cell Biol.* **19**, 1–9 (2016).
54. Ogiwara, H. et al. Histone acetylation by CBP and p300 at double-strand break sites facilitates SWI/SNF chromatin remodeling and the recruitment of non-homologous end joining factors. *Oncogene* **30**, 2135–2146 (2011).
55. Douglas, P., Gupta, S., Morrice, N., Meek, K. & Lees-Miller, S. P. DNA-PK-dependent phosphorylation of Ku70/80 is not required for non-homologous end joining. *DNA Repair (Amst.)* **4**, 1006–1018 (2005).
56. Jeong, J. et al. SIRT1 promotes DNA repair activity and deacetylation of Ku70. *Exp. Mol. Med.* **39**, 8–13 (2007).
57. Lin, Y. H. et al. KAP1 deacetylation by SIRT1 promotes non-homologous end-joining repair. *PLoS One* **10**, e0123935 (2015).
58. Morishita, H., Kaizuka, T., Hama, Y. & Mizushima, N. A new probe to measure autophagic flux in vitro and in vivo. *Autophagy* **13**, 757–758 (2017).
59. Liang, Q. et al. Zika virus NS4A and NS4B proteins deregulate Akt-mTOR signaling in human fetal neural stem cells to inhibit neurogenesis and induce autophagy. *Cell Stem Cell* **19**, 663–671 (2016).
60. Hou, P. et al. The ORF7a protein of SARS-CoV-2 initiates autophagy and limits autophagosome-lysosome fusion via degradation of SNAP29 to promote virus replication. *Autophagy* **19**, 551–569 (2023).
61. Miao, G. et al. ORF3a of the COVID-19 virus SARS-CoV-2 blocks HOPS complex-mediated assembly of the SNARE complex required for autolysosome formation. *Dev. Cell* **56**, 427–442.e425 (2021).
62. Dolata, K. M. et al. CP204L is a multifunctional protein of African swine fever virus that interacts with the VPS39 subunit of the homotypic fusion and vacuole protein sorting complex and promotes lysosome clustering. *J. Virol.* **97**, e0194322 (2023).
63. Overby, A. K., Popov, V. L., Niedrig, M. & Weber, F. Tick-borne encephalitis virus delays interferon induction and hides its double-stranded RNA in intracellular membrane vesicles. *J. Virol.* **84**, 8470–8483 (2010).
64. Jiang, D. et al. Identification of five interferon-induced cellular proteins that inhibit west nile virus and dengue virus infections. *J. Virol.* **84**, 8332–8341 (2010).
65. Fares, M. et al. Pathological modeling of TBEV infection reveals differential innate immune responses in human neurons and astrocytes that correlate with their susceptibility to infection. *J. Neuroinflammation* **17**, 76 (2020).
66. Selinger, M. et al. Integrative RNA profiling of TBEV-infected neurons and astrocytes reveals potential pathogenic effectors. *Computational Struct. Biotechnol. J.* **20**, 2759–2777 (2022).
67. Tsai, Y. T., Chang, S. Y., Lee, C. N. & Kao, C. L. Human TLR3 recognizes dengue virus and modulates viral replication in vitro. *Cell Microbiol* **11**, 604–615 (2009).
68. Hamel, R. et al. Biology of Zika virus infection in human skin cells. *J. Virol.* **89**, 8880–8896 (2015).
69. Miorin, L., Albornoz, A., Baba, M. M., D'Agaro, P. & Marcello, A. Formation of membrane-defined compartments by tick-borne encephalitis virus contributes to the early delay in interferon signaling. *Virus Res* **163**, 660–666 (2012).
70. Kindberg, E. et al. A functional toll-like receptor 3 gene (TLR3) may be a risk factor for tick-borne encephalitis virus (TBEV) infection. *J. Infect. Dis.* **203**, 523–528 (2011).
71. Mickienė, A. et al. Polymorphisms in chemokine receptor 5 and Toll-like receptor 3 genes are risk factors for clinical tick-borne encephalitis in the Lithuanian population. *PLoS One* **9**, e106798 (2014).
72. Dang, J. et al. Zika virus depletes neural progenitors in human cerebral organoids through activation of the innate immune receptor TLR3. *Cell Stem. Cell* **19**, 258–265 (2016).
73. Belin, S. et al. Uncoupling ribosome biogenesis regulation from RNA polymerase I activity during herpes simplex virus type 1 infection. *RNA* **16**, 131–140 (2010).
74. Ponti, D., Troiano, M., Bellenchi, G. C., Battaglia, P. A. & Gigliani, F. The HIV Tat protein affects processing of ribosomal RNA precursor. *BMC Cell Biol.* **9**, 32 (2008).
75. Devhare, P., Meyer, K., Steele, R., Ray, R. B. & Ray, R. Zika virus infection dysregulates human neural stem cell growth and inhibits differentiation into neuroprogenitor cells. *Cell Death Dis.* **8**, e3106 (2017).
76. Hammack, C. et al. Zika Virus Infection Induces DNA Damage Response in Human Neural Progenitors That Enhances Viral Replication. *J. Virol.* **93**, e00638–19 (2019).
77. Deng, J.-J. et al. Interplay between SIRT1 and hepatitis B virus X protein in the activation of viral transcription. *Biochimica et. Biophysica Acta (BBA) - Gene Regulatory Mechanisms* **1860**, 491–501 (2017).
78. Kwon, H. S. et al. Human immunodeficiency virus type 1 Tat protein inhibits the SIRT1 deacetylase and induces T cell hyperactivation. *Cell Host Microbe* **3**, 158–167 (2008).
79. Zhang, H. S., Chen, X. Y., Wu, T. C., Sang, W. W. & Ruan, Z. MiR-34a is involved in Tat-induced HIV-1 long terminal repeat (LTR) transactivation through the SIRT1/NFκB pathway. *FEBS Lett.* **586**, 4203–4207 (2012).
80. Bílý, T. et al. Electron tomography analysis of tick-borne encephalitis virus infection in human neurons. *Sci. Rep.* **5**, 10745 (2015).
81. Tavčar Verdev, P. et al. In human astrocytes neurotropic flaviviruses increase autophagy, yet their replication is autophagy-independent. *Cell. Mol. Life Sci.* **79**, 566(2022).
82. Liu, Z. et al. Transient activation of the PI3K-AKT pathway by hepatitis C virus to enhance viral entry. *J. Biol. Chem.* **287**, 41922–41930 (2012).
83. Kuroda, M., Halfmann, P. & Kawaoka, Y. HER2-mediated enhancement of Ebola virus entry. *PLoS Pathog.* **16**, e1008900 (2020).
84. Bouhaddou, M. et al. The global phosphorylation landscape of SARS-CoV-2 infection. *Cell* **182**, 685–712.e619 (2020).
85. Chu, J. J. & Yang, P. L. c-Src protein kinase inhibitors block assembly and maturation of dengue virus. *Proc. Natl Acad. Sci. USA* **104**, 3520–3525 (2007).
86. Alfhili, M. A., Alsughayyir, J., McCubrey, J. A. & Akula, S. M. GSK-3-associated signaling is crucial to virus infection of cells. *Biochim Biophys. Acta Mol. Cell Res* **1867**, 118767 (2020).
87. Nguyen, T. B. et al. Glycogen synthase kinase-3beta (GSK-3beta) inhibitors AR-A014418 and B6B3O prevent human immunodeficiency virus-mediated neurotoxicity in primary human neurons. *J. Neurovirol.* **15**, 434–438 (2009).
88. Sarhan, M. A., Abdel-Hakeem, M. S., Mason, A. L., Tyrrell, D. L. & Houghton, M. Glycogen synthase kinase 3β inhibitors prevent hepatitis C virus release/assembly through perturbation of lipid metabolism. *Sci. Rep.* **7**, 2495 (2017).
89. Edwards, T. G., Bloom, D. C. & Fisher, C. The ATM and Rad3-Related (ATR) Protein kinase pathway is activated by herpes simplex virus 1 and required for efficient viral replication. *J. Virol.* **92**, e01884–17 (2018).
90. Garcia, G. Jr. et al. Antiviral drug screen identifies DNA-damage response inhibitor as potent blocker of SARS-CoV-2 replication. *Cell Rep.* **35**, 108940 (2021).

91. Ahmadi, A. & Moradi, S. In silico analysis suggests the RNAi-enhancing antibiotic enoxacin as a potential inhibitor of SARS-CoV-2 infection. *Sci. Rep.* **11**, 10271 (2021).
92. Xu, Y. P. et al. Zika virus infection induces RNAi-mediated antiviral immunity in human neural progenitors and brain organoids. *Cell Res.* **29**, 265–273 (2019).
93. Gioia, U. et al. Pharmacological boost of DNA damage response and repair by enhanced biogenesis of DNA damage response RNAs. *Sci. Rep.* **9**, 6460 (2019).
94. Farias, K. J., Machado, P. R., Muniz, J. A., Imbeloni, A. A. & da Fonseca, B. A. Antiviral activity of chloroquine against dengue virus type 2 replication in Aotus monkeys. *Viral Immunol.* **28**, 161–169 (2015).
95. Zhang, S. et al. Chloroquine inhibits endosomal viral RNA release and autophagy-dependent viral replication and effectively prevents maternal to fetal transmission of Zika virus. *Antivir. Res* **169**, 104547 (2019).
96. Li, X. et al. Molecular detection and phylogenetic analysis of tick-borne encephalitis virus in ticks in northeastern China. *J. Med. Virol.* https://doi.org/10.1002/jmv.27303 (2021).
97. Hung, S. Y., Huang, W. P., Liou, H. C. & Fu, W. M. Autophagy protects neuron from Abeta-induced cytotoxicity. *Autophagy* **5**, 502–510 (2009).
98. Wang, Q. et al. Tamoxifen enhances stemness and promotes metastasis of ERα36(+) breast cancer by upregulating ALDH1A1 in cancer cells. *Cell Res.* **28**, 336–358 (2018).
99. Warnecke, A., Sandalova, T., Achour, A. & Harris, R. A. PyTMs: a useful PyMOL plugin for modeling common post-translational modifications. *BMC Bioinforma.* **15**, 370 (2014).
100. Jo, S., Vargyas, M., Vasko-Szedlar, J., Roux, B. & Im, W. PBEQ-Solver for online visualization of electrostatic potential of biomolecules. *Nucleic acids Res.* **36**, W270–W275 (2008).
101. Casado, P. et al. Kinase-substrate enrichment analysis provides insights into the heterogeneity of signaling pathway activation in leukemia cells. *Sci. Signal* **6**, rs6 (2013).
102. Horn, H. et al. KinomeXplorer: an integrated platform for kinome biology studies. *Nat. Methods* **11**, 603–604 (2014).
103. Hornbeck, P. V. et al. PhosphoSitePlus, 2014: mutations, PTMs and recalibrations. *Nucleic acids Res.* **43**, D512–D520 (2015).
104. Collins, A. et al. Measuring DNA modifications with the comet assay: a compendium of protocols. *Nat. Protoc.* **18**, 929–989 (2023).

Acknowledgements

This work was supported by grant from the National Natural Science Foundation of China (Grant No. 82302516, L.S.; 82372250, Q.L.; U23A20269, G.W.; 82341105, Q.L.), Jilin Province Science and Technology Innovation Research Institute Collaborative Innovation Project (Grant No. 20240207010CX,Y.C.Z.), Natural Science Foundation of Jilin Province (Grant No. YDZJ202301ZYTS431, L.S.), Scientific Research Project of Jilin Provincial Department of Education (Grant No. JJKH20231206KJ, L.S.), the Medical Innovation Team Project of Jilin University (Grant No.2022JBGS02, Q.L.), State Key Laboratory for Diagnosis and Treatment of Severe Zoonotic Infectious Diseases (Grant No. 2024ZZ00002, Q.L.; RCGHCRB202405, Y.C.Z.), and Norman Bethune Plan Project of Jilin University (Grant No. 2024B29, L.S.).

Author contributions

Q.L., Y.C.Z., L.S., and G.W. designed and supervised the project. W.W., X.G., Y.Z., T.T., J.Z., Y.X., H.C., H.X., and W.X. performed experiments and analyzed data. H.W., N.L., L.Z., G.S., Z.W., K.Z., and L.C. interpreted the results. L.S. wrote the original manuscript. Y.C.Z., G.W., and Q.L. revised the manuscript. All authors reviewed and proofread the manuscript.

Competing interests

The authors declare no conflicts of interest.

Additional information

Supplementary information The online version contains supplementary material available at https://doi.org/10.1038/s41467-024-54628-w.

Correspondence and requests for materials should be addressed to Yicheng Zhao, Guoqing Wang or Quan Liu.

Peer review information *Nature Communications* thanks Alessandro Marcello and the other, anonymous, reviewer(s) for their contribution to the peer review of this work. A peer review file is available.